

# Deep Learning for Retinal Degeneration Assessment: A Comprehensive Analysis of the MARIO , Challenge

Rachid Zeghlache<sup>a,c,\*</sup>, Ikram Brahim<sup>a,h</sup>, Pierre-Henri Conze<sup>a,c</sup>, Mathieu Lamard<sup>a,b</sup>, Mohammed El Amine Lazouni<sup>e</sup>, Zineb Aziza Elaouaber<sup>e,f</sup>, Leila Ryma Lazouni<sup>e</sup>, Christopher Nielsen<sup>r,s</sup>, Ahmad O. Ahsan<sup>r,s</sup>, Matthias Wilms<sup>r,t,u,v,w,x</sup>, Nils D. Forkert<sup>r,t,u,y</sup>, Lovre Antonio Budimir<sup>q</sup>, Ivana Matovinović<sup>q</sup>, Donik Vršnak<sup>q</sup>, Sven Lončarić<sup>q</sup>, Philippe Zhang<sup>a,k</sup>, Weili Jiang<sup>l</sup>, Yihao Li<sup>ai</sup>, Yiding Hao<sup>i</sup>, Markus Frohmann<sup>p</sup>, Patrick Binder<sup>p</sup>, Marcel Huber<sup>p</sup>, Taha Emre<sup>m</sup>, Teresa Finisterra Araújo<sup>m</sup>, Marzieh Oghbaie<sup>m</sup>, Hrvoje Bogunović<sup>m</sup>, Amerens A. Bekkers<sup>n</sup>, Nina M. van Liebergen<sup>n</sup>, Hugo J. Kuijff<sup>n,o</sup>, Abdul Qayyum<sup>ag</sup>, Moona Mazher<sup>ah</sup>, Steven A. Niederer<sup>ag</sup>, Alberto J. Beltrán-Carrero<sup>ac</sup>, Juan J. Gómez-Valverde<sup>ac,ad</sup>, Javier Torresano-Rodríguez<sup>ae</sup>, Álvaro Caballero-Sastre<sup>ac</sup>, María J. Ledesma Carbayo<sup>ac,ad</sup>, Yosuke Yamagishi<sup>j</sup>, Yi Ding<sup>af</sup>, Robin Peretzke<sup>z,aa</sup>, Alexandra Ertl<sup>z,aa</sup>, Maximilian Fischer<sup>z,aa</sup>, Jessica Kächele<sup>z,aa,ab</sup>, Sofiane Zehar<sup>f</sup>, Karim Boukli Hacene<sup>f</sup>, Thomas Monfort<sup>d</sup>, Béatrice Cochener<sup>a,b,g</sup>, Mostafa El Habib Daho<sup>a,b,1</sup>, Anas-Alexis Benyoussef<sup>d,1</sup>, Gwénéolé Quéllec<sup>a</sup>

<sup>a</sup>LaTIM UMR 1101, Inserm, Brest, France

<sup>b</sup>University of Western Brittany, Brest, France

<sup>c</sup>IMT Atlantique, Brest, France

<sup>d</sup>Service d'Ophthalmologie, CHRU Brest, Brest, France

<sup>e</sup>University of Tlemcen, Algeria

<sup>f</sup>LAZOUNI Ophthalmology Clinic, Tlemcen, Algeria

<sup>g</sup>Ophthalmology Department, CHRU Brest, Brest, France

<sup>h</sup>INSERM U1227 Lymphocytes B et Autoimmunité (LBAI), Brest, France

<sup>i</sup>Imperial College London, United Kingdom

<sup>j</sup>Division of Radiology and Biomedical Engineering, Graduate School of Medicine, The University of Tokyo, Tokyo, Japan

<sup>k</sup>Evolucare Technologies, France

<sup>l</sup>College of Computer Science, Sichuan University, China

<sup>m</sup>Medical University of Vienna, Austria

<sup>n</sup>TNO, The Hague, The Netherlands

<sup>o</sup>Image Sciences Institute, UMC Utrecht, Utrecht, The Netherlands

<sup>p</sup>Johannes Kepler University Linz, Austria

<sup>q</sup>University of Zagreb, Faculty of Electrical Engineering and Computing, Croatia

<sup>r</sup>Department of Radiology, University of Calgary, Calgary, AB, Canada

<sup>s</sup>Biomedical Engineering Graduate Program, University of Calgary, Calgary, AB, Canada

<sup>t</sup>Hotchkiss Brain Institute, University of Calgary, Calgary, AB, Canada

<sup>u</sup>Alberta Children's Hospital Research Institute, University of Calgary, Calgary, AB, Canada

<sup>v</sup>Department of Pediatrics, University of Calgary, Calgary, AB, Canada

<sup>w</sup>Department of Community Health Sciences, University of Calgary, Calgary, AB, Canada

<sup>x</sup>Department of Clinical Neuroscience, University of Calgary, Calgary, AB, Canada

<sup>y</sup>University of Calgary, Calgary, AB, Canada

<sup>z</sup>German Cancer Research Center (DKFZ) Heidelberg, Division of Medical Image Computing, Germany

<sup>aa</sup>Medical Faculty Heidelberg, Heidelberg University, Germany

<sup>ab</sup>German Cancer Consortium (DKTK), DKFZ, Germany

<sup>ac</sup>Biomedical Image Technologies (BIT), ETSI Telecomunicación, Universidad Politécnica de Madrid, Spain

<sup>ad</sup>Centro de Investigación Biomédica en Red de Bioingeniería, Biomateriales y Nanomedicina (CIBER-BBN), Madrid, Spain

<sup>ae</sup>Ophthalmology Service of the Provincial Ophthalmic Institute, Hospital Universitario Gregorio Marañón, Madrid, Spain

<sup>af</sup>University of Edinburgh, Scotland

<sup>ag</sup>National Heart and Lung Institute, Faculty of Medicine, Imperial College London, United Kingdom

<sup>ah</sup>Hawkes Institute, Department of Computer Science, University College London, London, United Kingdom

<sup>ai</sup>United Imaging Healthcare, China

## Abstract

The MARIO challenge, held at MICCAI 2024, focused on advancing the automated detection and monitoring of age-related macular degeneration (AMD) through the analysis of optical coherence tomography (OCT) images. Designed to evaluate algorithmic performance in detecting neovascular activity changes within AMD, the challenge incorporated unique multi-modal datasets. The primary dataset, sourced from Brest, France, was used by participating teams to train and test their models. The final ranking was determined based on performance on this dataset. An auxiliary dataset from Algeria was used post-challenge to evaluate population and device shifts from submitted solutions. Two tasks were involved in the MARIO challenge. The first one was the classification of evolution between two consecutive 2D OCT B-scans. The second one was the prediction of future AMD evolution over three months for patients undergoing anti-vascular endothelial growth factor (VEGF) therapy. Thirty-five teams participated, with the top 12 finalists presenting their methods. This paper outlines the challenge's structure, tasks, data characteristics, and winning methodologies, setting a benchmark for AMD monitoring using OCT, infrared imaging, and clinical data (such as the number of visits, age, gender, etc.). The results of this challenge indicate that artificial intelligence (AI) performs as well as a physician in measuring AMD progression (Task 1) but is not yet able of predicting future evolution (Task 2).

**Keywords:** MARIO challenge, AMD, MICCAI challenge, OCT, Disease progression

## 1. Introduction

Age-related macular degeneration (AMD) represents one of the leading causes of irreversible visual impairment worldwide, affecting approximately 196 million people globally (Schultz et al., 2021). This progressive neurodegenerative retinal disease primarily impacts individuals over 65 years of age, causing substantial central vision loss while typically preserving peripheral vision. AMD manifests across a spectrum of severity, with advanced stages geographic atrophy (GA) and neovascular AMD (AMD) affecting approximately 20% of patients and constituting the predominant cause of severe visual impairment in developed nations (Wong et al., 2014; Fleckenstein et al., 2018). The multifactorial etiology of AMD, involving complex interactions between genetic susceptibility and environmental risk factors, presents significant challenges for both prevention strategies and therapeutic interventions.

The introduction of anti-vascular endothelial growth factor (anti-VEGF) therapies in 2007 revolutionized the management of AMD, demonstrating unprecedented efficacy in halting disease progression and, in some cases, restoring visual function (Rosenfeld et al., 2006; Brown et al., 2006). However, the success of anti-VEGF therapy is contingent upon early diagnosis, accurate disease activity assessment, and strategic treatment planning based on regular monitoring. Optical coherence tomography (OCT) has emerged as the cornerstone imaging modality in this context, providing high-resolution, three-dimensional visualization of retinal microstructure capable of detecting critical exudative markers subretinal fluid (SRF), intraretinal fluid (IRF), and intraretinal hyperreflective foci which serve as main indicators of neovascular activity (Fig.1).

While artificial intelligence (AI) algorithms have demonstrated promising capabilities in identifying early and intermediate AMD stages and in predicting progression to advanced disease (Yim et al., 2020; Grassmann et al., 2018), a significant gap exists in AI applications specifically designed for longitudinal monitoring of neovascular activity in patients undergoing anti-VEGF therapy. Current research has predominantly focused on cross-sectional disease classification rather than the dynamic assessment required to detect subtle temporal changes in exudative activity, information crucial for optimizing individualized treatment regimens. Developing algorithms able to accurately characterize

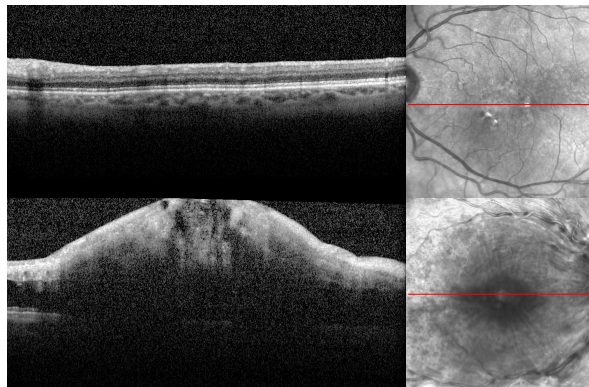


Figure 1: Representative OCT images illustrating normal retinal architecture (top) versus advanced neovascular AMD with characteristic pathological features including subretinal fluid and retinal pigment epithelium disruption (bottom).

disease evolution in these patients could substantially enhance treatment outcomes by enabling more precise, personalized anti-VEGF therapy protocols that respond directly to fluctuations in disease activity (Schmidt-Erfurth et al., 2022).

The MARIO (Monitoring Age-Related macular degeneration with Intelligent Ophthalmology) challenge<sup>2</sup> directly addresses this critical need by evaluating existing and novel AI algorithms specifically for detecting the evolution of neovascular activity in patients with exudative AMD. This initiative provides a diverse OCT dataset encompassing patients from both African and European populations, thereby facilitating assessment of domain generalizability and encouraging development of AI models capable of individualized disease monitoring across demographically diverse populations. By specifically targeting the progression dynamics of AMD in closely monitored clinical scenarios, this challenge aims to establish new benchmarks for AI in longitudinal disease management, ultimately contributing to more precise, equitable, and effective treatment strategies.

To provide a comprehensive roadmap for the reader, this paper is structured as follows:

Sect.2 reviews related work, contextualizing the challenge within the broader landscape of existing research and previous competitions. Sect.3 introduces the MARIO challenge in detail, outlining its specific objectives, clinical significance, and the particular problems it addresses. Sect.4 describes the dataset composition and characteristics, including acquisition protocols, pre-

\*Corresponding author:

Email address: rachid.zeghlache@imt-atlantique.fr ()

<sup>1</sup>These authors contributed equally.

<sup>2</sup>[https://youvenz.github.io/MARIO\\_challenge.github.io/](https://youvenz.github.io/MARIO_challenge.github.io/)

processing methodologies, and inherent limitations. It also presents the evaluation metrics employed to assess algorithmic performance. Sect.5, which provides a detailed summary of the methodologies proposed by each participating team. Sect.6 presents the results and outcomes of the competition, followed by A comprehensive comparison of results across different approaches. While Sect. 7 offers a critical discussion of key insights, limitations, and promising directions for future research.

## 2. Related work

### 2.1. Anti-VEGF treatment paradigms

Current anti-VEGF treatment strategies for AMD follow several established paradigms, including fixed-interval dosing, pro re nata (PRN, as needed), and treat-and-extend protocols (Lanzetta et al., 2021). Each approach presents distinct advantages and limitations regarding treatment burden, visual outcomes, and healthcare resource utilization. The fixed-interval dosing regimen, derived from pivotal clinical trials like MARINA and ANCHOR (Rosenfeld et al., 2006; Brown et al., 2006), involves regular monthly injections regardless of disease activity. While this approach provides optimal visual outcomes, it imposes substantial treatment burden on patients and healthcare systems. Conversely, the PRN approach involves treatment only when active disease is detected during monthly monitoring visits, reducing injection frequency but requiring frequent clinical assessment (Lalwani et al., 2009). The treat-and-extend protocol, which has gained prominence in recent years, aims to optimize the treatment-monitoring balance by gradually extending the interval between treatments when disease stability is achieved, and shortening intervals when recurrent activity is detected (Freund et al., 2015). This personalized approach necessitates accurate and consistent evaluation of disease activity markers, particularly fluid presence and evolution. This is precisely the clinical need that the MARIO challenge addresses.

### 2.2. Clinical significance of fluid dynamics

The presence, location, and quantity of retinal fluid serve as primary biomarkers for AMD activity and treatment response (Schmidt-Erfurth et al., 2018). Different fluid compartments—subretinal fluid (SRF), intraretinal fluid (IRF), and sub-retinal pigment epithelium fluid—exhibit distinct associations with visual outcomes and treatment response patterns. Studies

have demonstrated that persistent IRF strongly correlates with poorer visual outcomes and may indicate irreversible retinal damage (Blumenkranz et al., 2010; Sharma et al., 2016), while moderate SRF may be tolerated without significant visual impact in some patients (Guymer et al., 2019). This nuanced understanding of fluid dynamics has led to more sophisticated treatment decision-making, moving beyond binary dry/wet classification toward quantitative assessment of specific fluid patterns and their evolution over time. The development of AI algorithms able to detect subtle changes in fluid distribution and volume across sequential visits therefore addresses a critical unmet need in clinical practice: the ability to objectively quantify disease activity dynamics and personalize treatment decisions based on individual response patterns rather than on standardized protocols.

### 2.3. Technical challenges in longitudinal OCT analysis

The development of robust algorithms for longitudinal OCT analysis in AMD presents several unique technical challenges that are distinct from conventional cross-sectional classification or segmentation tasks.

#### 2.3.1. Registration and alignment

Accurate spatial alignment between sequential OCT volumes is fundamental for reliable detection of temporal changes. Patient movement, variations in scan protocols, and alterations in retinal morphology due to disease progression or treatment effects can complicate registration (Lang et al., 2016). While commercial OCT systems incorporate basic eye-tracking functionality, suboptimal alignment remains common in clinical datasets. Advanced registration techniques are required to establish precise spatial correspondence across sequential scans. These approaches must account for both global transformation parameters and local deformations resulting from disease activity changes. Methods ranging from feature-based registration to deformable transformation models have been explored, though their application in routine clinical analysis remains limited (Golabbakhsh and Rabbani, 2013).

#### 2.3.2. Handling irregular time intervals

Clinical follow-up schedules in AMD management frequently involve irregular time intervals between visits, with intervals ranging from 4 weeks to several months depending on disease activity and treatment protocol. This temporal irregularity poses significant challenges for conventional sequence modeling approaches, which typically assume uniform sampling intervals. Recent deep learning approaches have adapted to address

this challenge, including temporal convolutional networks with dilated convolutions (Lea et al., 2017), continuous-time models like neural ordinary differential equations (NODEs) (Chen et al., 2018), and attention-based architectures that can model long-range dependencies regardless of temporal distance (Vaswani et al., 2017). The MARIO challenge provides an opportunity to evaluate these approaches in a standardized clinical context.

### 2.3.3. *Balancing sensitivity and specificity*

The clinical utility of AMD monitoring algorithms depends on achieving an optimal balance between sensitivity (detecting all instances of disease activity) and specificity (avoiding false positive detections that could lead to unnecessary treatment). This balance is particularly crucial in treatment decision-making, where false negatives could result in undertreatment and disease progression, while false positives might lead to overtreatment and increased iatrogenic risks (Liu et al., 2019). Conventional evaluation metrics like accuracy may be insufficient or even misleading in this context, particularly when dealing with class imbalance or when considering the differential clinical impact of various error types. The MARIO challenge therefore incorporates clinically relevant evaluation metrics that reflect the actual utility of algorithms in treatment decision support.

Research in AI-assisted AMD analysis using OCT imaging has evolved substantially in recent years, focusing on several interconnected domains (Cricoli et al., 2024; Romond et al., 2021; Muntean et al., 2023; Schmidt-Erfurth et al., 2016): automated retinal layer segmentation, detection and quantification of exudative features, longitudinal analysis of disease progression, and cross-domain generalizability. These research directions collectively provide the foundation for comprehensive understanding of AMD pathophysiology and evidence-based clinical decision-making. We review these key areas with particular emphasis on their relevance to monitoring disease progression in patients undergoing anti-VEGF treatments.

### 2.3.4. *Exudative feature detection and quantification*

The detection and precise quantification of exudative markers including SRF, IRF, and hyperreflective foci - represents a critical component in evaluating neovascular AMD activity, as these features directly inform anti-VEGF treatment decisions and retreatment intervals. Early approaches relied on traditional computer vision techniques with handcrafted feature extraction, but deep learning architectures have since transformed the landscape of exudative feature detection (Hassan

et al., 2021; Schlegl et al., 2018). Convolutional neural networks, particularly implementations of mask R-CNN, U-Net derivatives, and DenseNet-based architectures, have significantly improved accuracy in identifying and segmenting fluid compartments and hyperreflective material (Venhuizen et al., 2018). However, these models continue to face challenges with variations in image quality, scan protocols, and patient-specific anatomical differences. Recent advancements have explored specialized architectural adaptations, including attention mechanisms (Xu et al., 2023), Transformer-based models (Melinščak, 2023), and hybrid approaches that integrate anatomical priors with data-driven learning (Roy et al., 2017).

While these innovations have improved performance in controlled settings, the reliable detection of subtle fluid changes over time remains challenging, particularly in patients undergoing active treatment. The MARIO challenge format, with its focus on patients receiving ongoing anti-VEGF therapy, provides an ideal testbed for evaluating models capable of sensitive and specific fluid detection across sequential visits. This capability is crucial for longitudinal disease monitoring and capturing the temporal evolution of exudative markers, which directly impacts treatment decision-making (Schmidt-Erfurth et al., 2022; Simader et al., 2014).

### 2.3.5. *Longitudinal analysis and progression modeling*

Recent advances in longitudinal OCT analysis have enabled more sophisticated approaches to understanding and predicting AMD progression. Traditional methods relied primarily on statistical modeling of discrete time points, but contemporary approaches increasingly leverage the temporal continuity, inherent in disease progression.

Self-supervised learning techniques have demonstrated promise in modeling disease trajectories and predicting the onset of advanced AMD stages without requiring extensive labeled data (Rivail et al., 2019; Jung et al., 2024). These approaches enable the extraction of meaningful representations from temporal sequences of OCT volumes, capturing subtle changes that might escape human detection. Recurrent neural networks, particularly LSTM and GRU architectures, have been applied to model sequential dependencies in OCT data. However, they often struggle with irregular sampling intervals common in clinical practice (Lad et al., 2022).

More recently, differential equation-based models, especially NODEs, have emerged as powerful frameworks for modeling continuous-time disease dynamics in various conditions including AMD (Yellapragada et al., 2022; Chakravarty et al., 2024). These ap-

proaches offer distinct advantages in handling irregular sampling intervals and providing interpretable trajectories of disease states, allowing for more natural integration of multimodal data including imaging biomarkers and clinical factors.

Despite these advances, existing longitudinal models typically focus on predicting conversion to advanced disease rather than characterizing fluctuations in disease activity within patients already diagnosed with AMD. The MARIO challenge addresses this gap by specifically targeting the detection of disease activity changes in patients undergoing treatment, representing a more clinically relevant scenario for therapeutic decision-making.

### 2.3.6. Domain adaptation and generalizability

Cross-domain generalizability remains one of the most significant challenges in clinical OCT analysis for AMD (Kugelman et al., 2022; Matta et al., 2024). Substantial variability in OCT data can arise from differences in scanner types, acquisition protocols, image quality, and patient demographics, often resulting in significant performance degradation when algorithms are applied outside their training domain. Various domain adaptation techniques have been proposed to address these challenges, including adversarial learning approaches (Guan and Liu, 2021), transfer learning strategies (Liu et al., 2022), and generative models such as CycleGANs for style transfer between domains (Gomariz et al., 2022). These methods aim to reduce the domain shift between source and target distributions, thereby improving model robustness across heterogeneous data sources. However, the fundamental limitation of restricted data diversity persists in most current research, with algorithms developed and validated predominantly on homogeneous populations showing diminished performance when applied to underrepresented groups.

Addressing algorithmic bias is therefore essential for ensuring equitable performance across diverse populations (Ueda et al., 2024; Lim et al., 2024). The MARIO challenge uniquely addresses these limitations by providing a dataset inclusive of both African and European patient data, promoting the development of adaptable models suitable for global deployment in diverse clinical settings.

### 2.3.7. Publicly-available datasets and benchmarking efforts

Public datasets and standardized benchmarks have been instrumental in advancing AMD research, particularly in the domains of fluid detection and retinal

layer segmentation. Notable contributions include the RETOUCH challenge dataset (Bogunovic et al., 2019), which features OCT images from multiple devices and various retinal diseases, establishing important benchmarks for fluid detection and segmentation tasks. Similarly, the OCTAGON dataset (Díaz et al., 2019) provides valuable resources for algorithm development and validation in retinal OCT analysis. However, these existing datasets have limitations that restrict their utility for developing comprehensive AMD monitoring solutions. Most critically, they often lack:

- longitudinal data with sufficient temporal resolution to capture disease dynamics during treatment,
- geographic and demographic diversity needed to evaluate algorithm generalizability,
- standardized annotations of subtle changes in disease activity relevant to treatment decisions,
- integration of clinical metadata with imaging findings to provide contextual information.

The MARIO challenge addresses these limitations by establishing a unique benchmarking platform with several distinguishing features. First, it offers a dataset specifically designed to evaluate algorithms for monitoring disease progression in treated patients rather than simple binary classification or segmentation tasks. Second, it promotes equitable AI development by accounting for demographic variability across different geographic regions. Finally, it provides a standardized framework for evaluating algorithmic performance on clinically relevant outcomes related to disease activity changes. This initiative represents the first MICCAI-affiliated challenge specifically focused on AMD progression monitoring, providing a valuable resource for the research community. By offering participants the opportunity to test their methods on both European and African datasets, the challenge enables rigorous evaluation of algorithmic performance across shifted populations with respect to both ethnicity and OCT acquisition devices. This is a critical step toward developing truly generalizable solutions for global application.

## 3. Challenge description

The MARIO challenge is designed following the BIAS Reporting Guideline Maier-Hein et al. (2018) for enhanced quality and transparency of biomedical research. The proposal was approved after two rounds of MICCAI review followed by a call for participation

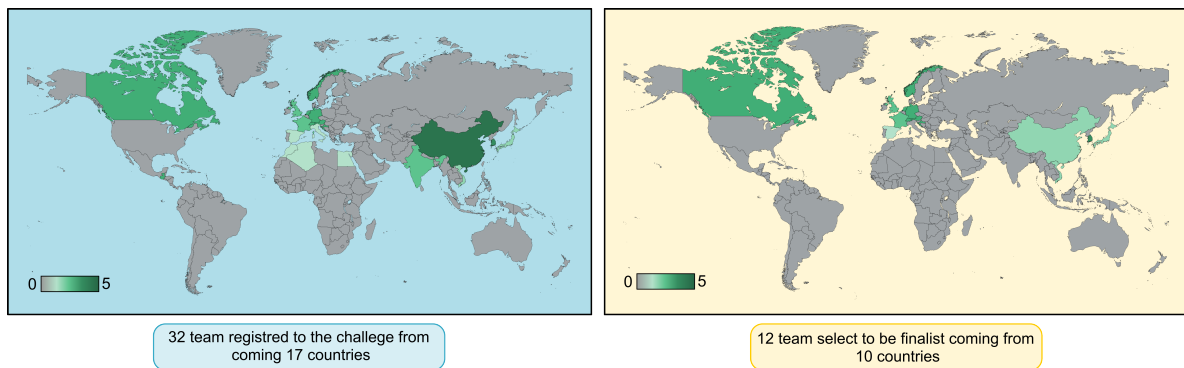


Figure 2: Distribution of participants registered to the challenge of both task and distribution of finalist and challenge participation statistics.

circulated online and offline. The challenge was officially launched on April 1, 2024, and run through a 6-months window as shown in Fig. 3 using the codabench platform for hosting Xu et al. (2022). This period is characterized by several activities, such as the release of training data, customized metrics library, slack communication channel, a snippet of “getting started” code, GitHub repositories, etc., to guide and support the participants’ method development. Fig.2 presents the numbers of teams and associated countries that register for the challenge and also the countries associated to the finalists. The participating teams develop their novel methods, fine-tune a state-of-the-art method, or improve on existing solutions during this period. The challenge timeline also involves a validation phase, harnessed by the use of a self-validation system, validation data samples, a Docker template, and guidelines provided to facilitate method submission. The whole process is concluded with the presentation of the method, results, and award winners at MICCAI 2024 conference in Marrakesh on October 10, 2024.

### 3.1. Challenge Format

The challenge comprised three phases:

- **Training Phase:** Release of training data for algorithm development.
- **Off-Site Validation:** Submission of results on validation data to determine finalists.
- **Final Round:** Top teams submitted Docker containers for on-site evaluation.

Participants addressed two core tasks:

### 3.2. Proposed tasks

The first task (described in Fig.4) was the classification of evolution between two consecutive 2D OCT B-scan.

The second task (described in Fig.5) was the prediction of future AMD evolution over three months for patients undergoing anti-VEGF therapy.

All submissions were evaluated based on F1-score, specificity, and Rk-correlation coefficients for both tasks, with an additional Quadratic Weighted Kappa metric for Task 2. Members of the organizer’s institutes could participate but were not eligible for awards. Regarding the publication policy, up to five 5 members of the individual top teams according to the leaderboard were invited to contribute to this joint challenge paper as co-authors up to five 3 members for the top 7-12, and the participating teams may publish their own results separately with citations to the assigned papers on the online challenge platform after the challenge paper is published. To access the training and testing datasets, participants first register on the challenge website and sign a non-disclosure contract on the usage of the datasets. Afterward, participants are provided with a download link to the online repository containing the dataset. For submission, the participants could perform cross validation on the training set. The evaluation code <sup>3</sup> was made available prior to submission. The participating teams were encouraged to make their source code publicly available.

## 4. Data description

The MARIO database, comprises a comprehensive longitudinal collection of ophthalmic data, facilitating

<sup>3</sup><https://github.com/YouvenZ/MARIO-Challenge-MICCAI-2024>

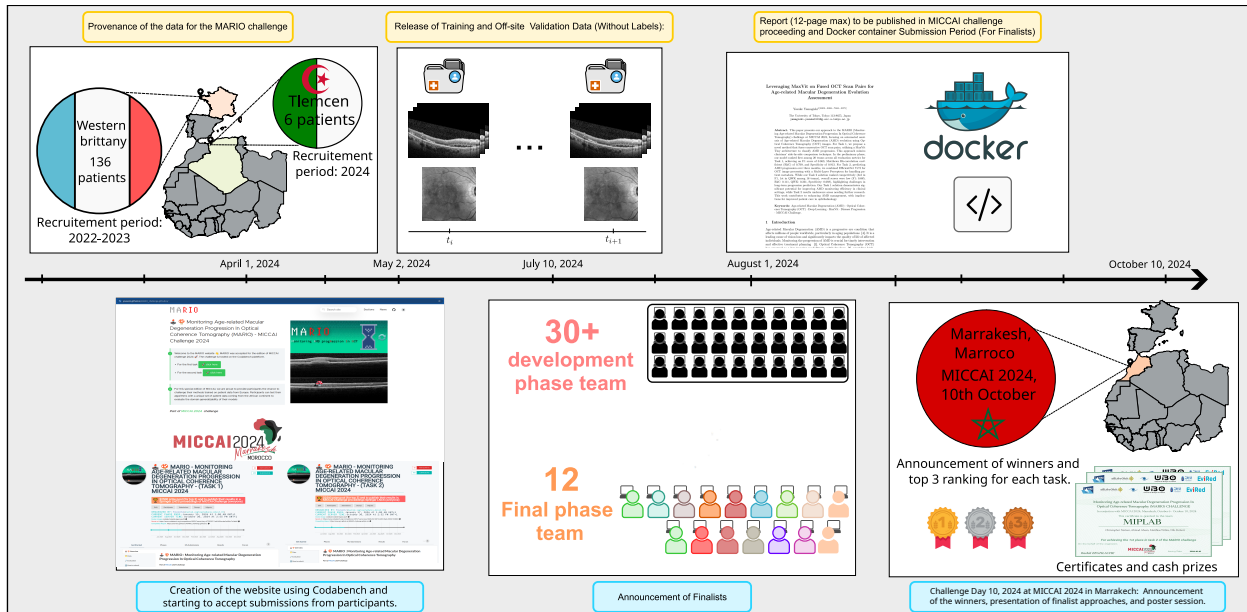


Figure 3: Time line of the challenge since inception.

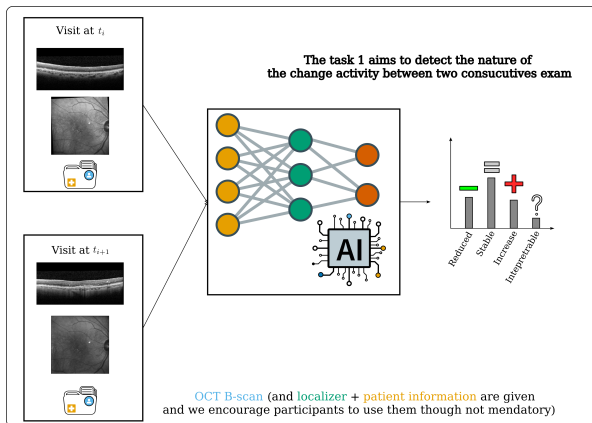


Figure 4: Illustration of goal associated to the task 1.

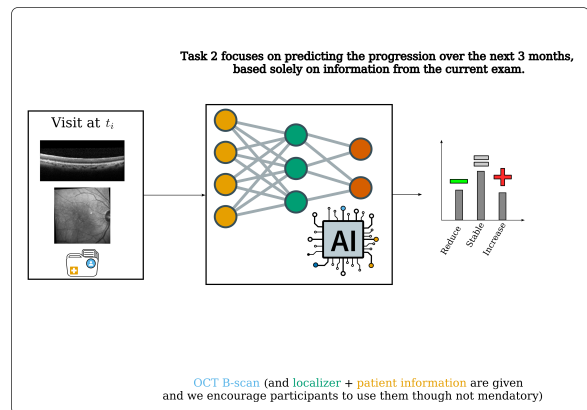


Figure 5: Illustration of goal associated to the task 2.

detailed analysis of AMD. As illustrated in Figure 6, the dataset's composition and characteristics provide a robust foundation for investigating disease progression and treatment efficacy. The gender distribution reveals a notable skew towards female patients, with 84 female participants compared to 52 male participants, suggesting a potential demographic bias in the patient population or a higher prevalence of AMD among females Rudnicka et al. (2012). The imaging frequency followed standardized protocols for most patients, with 785 examinations performed using 19 B-scans and 337 examinations using 25 B-scans. The observed variation

in B-scan count likely reflects differences in clinical assessments or adjustments to protocols tailored to individual patient needs. In terms of follow-up timing, the majority of patients demonstrated short inter-visit intervals, suggesting consistent and diligent monitoring. Nevertheless, the presence of outliers, with inter-visit periods extending to 1600 days, points to instances of irregular follow-up, possibly due to patient compliance issues or clinical scheduling limitations.

The age distribution at baseline demonstrates a concentration within the elderly population, a demographic typically associated with AMD. The mean age at base-

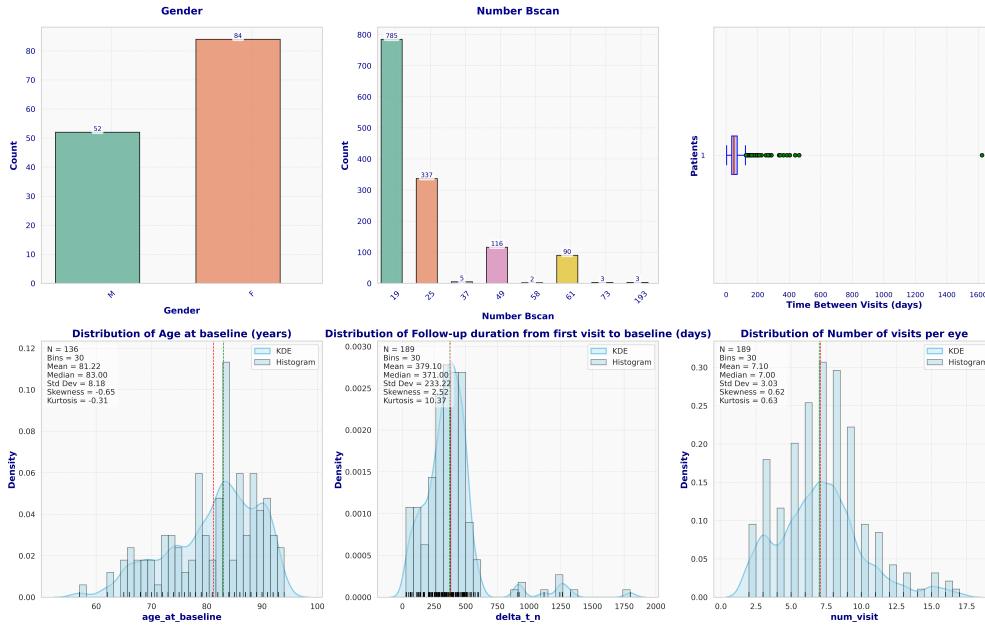


Figure 6: Illustration of exploratory data analysis MARIO database.

line was 81.22 years, with a median of 83 years, and the majority of patients falling within the 70-90 year age range. This age profile aligns with the known prevalence of AMD in older adults. The follow-up duration, calculated from the initial visit to the baseline, averaged 379.10 days, with a median of 371 days, signifying a substantial monitoring period. This longitudinal depth is essential for analyzing disease trajectories and evaluating long-term treatment outcomes.

Finally, the frequency of patient visits per eye, with a mean of 7.10 visits and a typical range of 4 to 10 visits, underscores the intensive clinical management required for AMD. This frequent monitoring regimen is indicative of the chronic and progressive nature of the disease, necessitating consistent evaluation and intervention. Collectively, these descriptive statistics provide a comprehensive overview of the MARIO database, highlighting its suitability for detailed investigation into the clinical dynamics of AMD.

#### 4.1. Data Pre-Processing

The XML metadata files were de-identified, and BMP images were converted to PNG format. Consecutive 3D volumes were registered using the device follow-up mode to account for patient movement. Inter-annotator agreement was established as a baseline for algorithm

evaluation, given the variability in distinguishing between stable and reduced activity.

#### 4.2. Manual annotation

For test cases, two ophthalmologists (A.B, T.M) performed the annotation independently. For training and validation cases, one ophthalmologist performed the annotation. An online annotation tool was designed for the study. Consecutive C-scans were viewed jointly on the same screen (older examination at the top, newer examination at the bottom). With a slider, the annotator could browse through pairs of matched B-scans from the two consecutive C-scans. Moreover, 5 patients (from the training set) were used to train the annotators. After annotating these 5 patients: 1) annotations were compared by the challenge organizers and presented to the annotators, 2) the organizers discussed their annotation strategy with each other and 3) they were given the opportunity to revise their annotations. Next, they annotated the remaining 131 patients independently. For each pair of matched B-scans, the annotator assigned one of the following 7 labels presented in Tab 1 along with their corresponding number of pairs.

#### 4.3. Simplified classification

The task proposed in this challenge focuses on pairs of 2-D slices (B-scans) from two consecutive OCT ac-

Name Class	Class Label	Number of Pairs
UNINTERPRETABLE	-1	2303
INACTIVE	0	18 852
ELIMINATED	1	2170
PERSISTENT REDUCED	2	2110
PERSISTENT STABLE	3	1289
PERSISTENT WORSENER	4	1238
APPEARED AND ELIMINATED	5	9
APPEARED	6	1876

Table 1: Data distribution of the manual annotation.

Name Class	Class Label	Number of Pairs
Reduced	0	4280
Stable	1	20 141
Worsened	2	3114
Other	-1	2312

Table 2: Data distribution of the simplified annotation

quisitions. The goal is to classify evolution between these two slices (‘before’ and ‘after’), which clinicians typically look at side by side on their screen. For the evolution assessment, three classes are defined based on the image level annotation presented in Tab 2 along with their corresponding number of pairs.

1. Reduced (class 0)
  - Contain labels: eliminated (1) or persistent reduced (2)
2. Stable (class 1)
  - Contain labels: inactive (0) or persistent stable (3)
3. Worsened (class 2)
  - Contain labels: persistent worsened (4) or appeared (6)

#### 4.4. Justification for dataset size

Data export was manual and, therefore, time-consuming. In addition, manually annotating thousands of image pairs by two retinal experts was also time-consuming. This was the reason for not collecting a larger dataset. However, this remains larger than a similar study published by one of the organizers Quellec et al. (2019), which involved 70 patients, as opposed to 136 here.

#### 4.5. Sources of errors from data and annotation

We observed two main sources of inter-annotator variability:

1. The distinction between an absence of disease activity and a stable activity (two types of non-evolution).
2. The distinction between an eliminated activity and a reduced (but not fully eliminated) activity. Experts disagreed for about 25% of the B-scan pairs.

Another source of error arose during image acquisition. The operator sometimes forgot to activate the follow-up mode, resulting in non-registered OCT volumes. This occurred in about 10% of consecutive acquisitions.

#### 4.6. Evaluation Metrics

The evaluation of algorithms in Task 1 and Task 2 relies on the following metrics:

- **F1-score:** Evaluates classification accuracy by balancing precision and recall, which is particularly relevant for handling class imbalances.
- **Specificity:** Measures the ability to correctly identify non-progression cases, ensuring a reliable detection of negative instances. Sensitivity is not emphasized here as the focus is on minimizing false positives rather than maximizing true positives.
- **Rank Correlation Coefficient:** Assesses the agreement between algorithmic predictions and human grading, which is crucial for ordinal classification tasks.
- **Quadratic Weighted Kappa** (Only for Task 2): Used to evaluate prediction accuracy for disease progression. This metric is relevant in Task 2 because it accounts for the ordinal nature of disease stages, penalizing larger misclassifications more heavily. However, it is not used in Task 1 since that task involves ordinal categories where alternative correlation-based metrics, such as the rank correlation coefficient, are more appropriate for assessing agreement.

## 5. Proposed solutions

A total of 35 teams participated, with 12 teams selected for the final phase as described in Fig.2. To be selected as a finalist, you should have submitted at least 5 unique submissions for both tasks and provided a better than the baseline that was provided in the leaderboard for the development phase.

### 5.1. Summary of methods proposed for each team

Table 3: Summary of the best methods for each finalist for task 1.

Team	Preprocessing	Backbone	Loss	Post processing	Data augmentation	Use of				Github link
						Pretext task	Foundation model	Multi-modality	Public dataset	
Lumine	Normalization, resize	Siamese network using ConvNeXt_large as backbone	Weighted cross-entropy	No	ColorJitter, GaussianBlur, RandomAffine, HorizontalFlip, GaussianNoise	N	Y/ConvNeXt_large	Y/multiple Siamese network	ImageNet (pre-trained weight from pytorch image models)	<a href="https://github.com/lumine-1/MARIO_Project">https://github.com/lumine-1/MARIO_Project</a>
yyama	concatenation, resize, normalization	MaxViT Tiny	CE	Ensembling of 5 folds CV	Random resized crop, Random horizontal flip, Random rotation, Coarse dropout	N	N	N	ImageNet (pre-trained weight from pytorch image models)	<a href="https://github.com/yamagishi0824/MARIO24-MaxViT-Fused">https://github.com/yamagishi0824/MARIO24-MaxViT-Fused</a>
DF41	OCTIP <sup>4</sup>	ResNet50	CE	Ensembling, (average)	RandomHorizontalFlip, RandomVerticalFlip, RandomRotation, ColorJitter, RandomPerspective, GaussianBlur	N	N	N	N	<a href="https://github.com/pzhangwj/mario_challenge_code">https://github.com/pzhangwj/mario_challenge_code</a>
Optima	crop, resize, normalization	RETFound (Large ViT)	Cross-entropy loss	Ensembling	rotation, horizontal flipping	SiamRETFound	Y/Simulated binary change detection task: change/no change	N	Kermany	<a href="https://github.com/EmreTaha/Siamese-EMD-for-AMD-Change">https://github.com/EmreTaha/Siamese-EMD-for-AMD-Change</a>
TONIC	Resampled image to 224x224	ResNet18	CE	-	Random horizontal and vertical flips, Rotations, Brightness/Contrast (using PyTorch ColorJitter), and Resized Cropping	N	N	Y/ two ResNet18s	ImageNet (ResNet18 is trained on the ImageNet dataset.)	<a href="https://github.com/ninamalou/TONIC-MICCAI-2024">https://github.com/ninamalou/TONIC-MICCAI-2024</a>
Jkstudents	crop, resize, normalization	ViT-B/14 distilled	CE	Ensembling on models trained on different patient ID-split folds	Resize to 224x224, normalization	N	<b>Y: ViT-B/14 distilled</b>	N	<b>Y (kind of): from pre-training foundation model only</b>	<a href="https://github.com/marceljhuber/mario-miccai2024">https://github.com/marceljhuber/mario-miccai2024</a>
FERLIV	resize, crop, normalization	ViT-Large	weighted CCE	-	random resized crop, horizontal flip	Y/Segmenter with Linear Decoder	Y/OCT RET-Found (in Pretext Task)	N	Y/OCT MS and Healthy Controls Data	<a href="https://github.com/LovreAB17/ferliv-mario">https://github.com/LovreAB17/ferliv-mario</a>
MIPLAB	Resize, intensity normalization	RETFound (ViT-large) + EfficientNetV2	Cross-entropy + hinge	Pseudolabelling	Horizontal/vertical flips, rotation, translation, contrast adjustments	Y/Masked autoencoder (via RET-Found)	Y/RET-Found	Y/Fusion of OCT + localizer + clinical variables	N	<a href="https://github.com/chrisnielsen/miccai-2024-mario-challenge">https://github.com/chrisnielsen/miccai-2024-mario-challenge</a>
MIC group 6	z-score Normalization, CenterCrop 224x224	ViT	CE	-	ResizedCrop, Rotation, HorizontalFlip, Rotation, Affine, GaussianBlur, GaussianNoise, GaussianBlur	N	Y/Biomed-Clip	Y/Biomed-clip	N	<a href="https://github.com/MIC-DKFZ/mario">https://github.com/MIC-DKFZ/mario</a>
STEP	3D volume creation, resize, normalization	Vision Transformer	Focal Loss	—	Intensity scaling, Gaussian noise, horizontal and vertical flip	—	Y/RET-Found	N	N	<a href="https://github.com/BIT-UPM/mario_miccai_24_step_amd">https://github.com/BIT-UPM/mario_miccai_24_step_amd</a>
scyyd4	crop, resize, normalization	ConvNeXt V2-Large	CE	Ensembling	Rotation, Zoom	N	Y/ConvNeXt V2-Large	N	N	<a href="https://github.com/YIDING4869/MARIO2024">https://github.com/YIDING4869/MARIO2024</a>
Cemrg	Resize, normalization	MobileNetV3	CE	Ensembling +TTA	Random rotations, Flips, Brightness adjustments, contrast variations	N	Y/MobileNetV3	N	N	<a href="https://github.com/RespectKnowledge/MARIO_DL_solution/tree/main">https://github.com/RespectKnowledge/MARIO_DL_solution/tree/main</a>

The following section provides a concise overview of the methodologies developed by each finalist team. To

facilitate understanding, a visual summary illustrating the common pipeline structures employed by the partic-

Table 4: Summary of the best methods for each finalist for task 2, N refer to No, and Y to yes.

Team	Preprocessing	Backbone	Loss	Post processing	Data augmentation	Use of				Github link
						Pretext task	Foundation model	Multi-modality	Public dataset	
Lumine	Normalization, resize	ConvNeXt_large	Weighted CE	Threshold-based label adjustment by localizer	ColorJitter, GaussianBlur, RandomAffine, HorizontalFlip, GaussianNoise	N	Y / ConvNeXt_large	N	Y / ImageNet (pre-trained weight from pytorch image models)	<a href="https://github.com/lumine-1/MARIO_Project">https://github.com/lumine-1/MARIO_Project</a>
yyama	concatenation, resize, normalization	EfficientNet V2	CE	N	Random resized crop, Random horizontal flip, Random rotation, Coarse dropout	N	N	Y / using Patient Meta-data	ImageNetk + 22K (pre-trained weight from pytorch image models)	<a href="https://github.com/yamagishi0824/MARIO24-MaxVit-Fused">https://github.com/yamagishi0824/MARIO24-MaxVit-Fused</a>
DF41	OCTIP*	ResNet50, ViT-Large (PP-MAE)	CE	Ensembling (average)	RandomHorizontalFlip, RandomVerticalFlip, RandomRotation, ColorJitter, RandomPerspective, GaussianBlur	N	N	N	N & Y / PMAE	<a href="https://github.com/pzhangvj/mario_challenge_code">https://github.com/pzhangvj/mario_challenge_code</a>
Optima	crop, resize, normalization	ViT16	Focal Loss + Wasserstein-2 Loss	Majority Voting	rotation, horizontal flipping	Y / MAE	N	N	N	<a href="https://github.com/EnreTaha/Siamese-EMD-for-AMD-Change">https://github.com/EnreTaha/Siamese-EMD-for-AMD-Change</a>
TONIC	Resampled image to 224x224	ResNet18	CE	Majority Voting	Random horizontal and vertical flips, Rotations, Brightness/Contrast (using PyTorch ColorJitter), and Resized Cropping	N	N	N	ImageNet (ResNet18 is trained on the ImageNet dataset.)	<a href="https://github.com/ninamalous/TONIC-MICCAI-2024">https://github.com/ninamalous/TONIC-MICCAI-2024</a>
Jkstudents	Resize to 224x224, normalization	RETFound	Neg. CosSim with predicted task 1 embeddings	-	Utilize dataset from task 1, setting preds. from class 3 to class 1	Y / Latent Matching with predicted embeddings using data from task 1	Y	N	Y (kind of): from pre-training foundation model only + task 1 data	<a href="https://github.com/marceljhuber/mario-miccai2024">https://github.com/marceljhuber/mario-miccai2024</a>
FERLIV	resize, crop, normalization	ViT-Large	weighted CCE	-	random resized crop, horizontal flip	Y / Task 1	Y / OCT RET-Found (in Pretext Task)	N	Y / MARIO Task 1 Dataset	<a href="https://github.com/LovraB17/ferliv-mario">https://github.com/LovraB17/ferliv-mario</a>
MIPLAB	Resize, intensity normalization	RETFound (ViT-large) + EfficientNetV2	CE + ordinal logistic classification loss	None	Horizontal/vertical flips, rotation, translation, contrast adjustments	Y / Masked autoencoder (via RET-Found)	Y / RET-Found	Y / Fusion of OCT + localizer + clinical variables	N	<a href="https://github.com/chrisnielsen/miccai-2024-mario-challenge">https://github.com/chrisnielsen/miccai-2024-mario-challenge</a>
MIC group 6	z-score Normalization, CenterCrop 224x224	ResNet50	CE	-	ResizedCrop, Rotation, HorizontalFlip, Rotation, Affine, GaussianBlur, GaussianNoise, GaussianBlur	N	Y / ImageNet	Y / ImageNet	N	<a href="https://github.com/MIC-DFK2/mario">https://github.com/MIC-DFK2/mario</a>
STEP	3D volume creation, resize, normalization	Vision Transformer	Focal Loss	—	Intensity scaling, Gaussian noise, horizontal and vertical flip	N	Y / RET-Found	N	N	<a href="https://github.com/BIT-UPM/mario_miccai_24_step_amd">https://github.com/BIT-UPM/mario_miccai_24_step_amd</a>
scyyd4	resize, normalization	ConvNeXt V2-Large (frozen to get features), CLAM SB	CE	Majority Voting	N	N	Y / ConvNeXt V2-Large, CLAM SB	N	N	<a href="https://github.com/YIDING4869/MARIO2024">https://github.com/YIDING4869/MARIO2024</a> , <a href="https://github.com/YIDING4869/MARIO2">https://github.com/YIDING4869/MARIO2</a>
Cemrg	Resize, normalization	MobileNetV3	CE	Ensembling +TTA	Random rotations, Flips, Brightness adjustments, contrast variations	N	Y / MobileNetV3	N	N	<a href="https://github.com/RespectKnowledge/MARIO_DL_solution/tree/main">https://github.com/RespectKnowledge/MARIO_DL_solution/tree/main</a>

ipants is presented in Figure Fig. 7. The detailed specific methodology of each team for Task 1 and Task 2 is documented in Tab. 3 and Tab. 4, respectively.

### 5.1.1. lumine - Team Summary

#### Task 1:

The Lumine team developed a deep learning model

designed to classify progression in Age-related Macular Degeneration (AMD) using OCT images captured over two consecutive sessions. The preprocessing methods include resize and Z-score normalization, each image was resized to 224x224 pixels to match the pre-trained network. To address data imbalance, we utilized data augmentation methods including ColorJitter, Gaus-

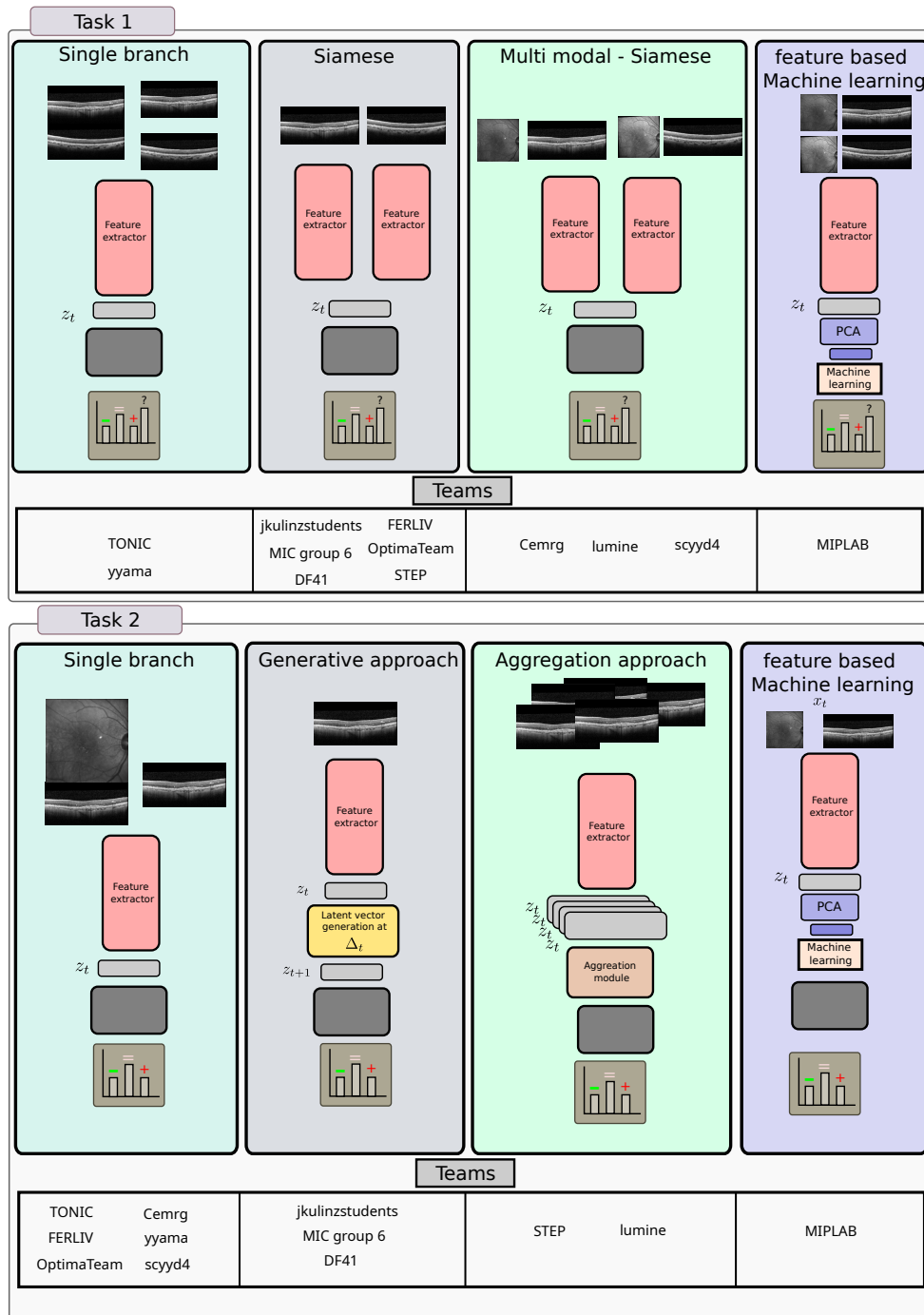


Figure 7: A comprehensive overview of the diverse methodologies proposed by participants for both tasks is presented, organized into four distinct meta-approach categories. Specifically, Task 1 solutions utilized single-head architectures, Siamese networks, multimodal Siamese networks, and feature-based machine learning algorithms. Task 2 implementations employed single-head models, generative methodologies, and feature-based machine learning techniques.

sianBlur, RandomAffine, HorizontalFlip, and Gaussian-Noise. These methods are not only used during train-

ing but also before training to generate different quantities of images for different classes to mitigate data im-

balance. For Task 1, a Siamese network was utilized, with both branches consisting of a ConvNeXt\_large feature extractor to process each image in a pair simultaneously. The model also incorporated a multi-head attention mechanism to better extract features. Final classification is derived by combining the extracted features and passing them through a linear classifier with ReLU activation. The training utilized the AdamW optimizer with learning rate decay, and cross-entropy loss with a balanced weighting scheme to counteract the class imbalance. Several models using different hyperparameters are trained and used to classify the image. Results produced by these networks are combined and weighted to produce the final classification result.

**Task 2:**

For Task 2, they utilized a standalone ConvNeXt\_large model to predict disease progression based on OCT scans taken three months apart. The preprocessing methods are also resize and Z-score normalization. To ensure the model was exposed to a wide variety of augmented samples, they also used data augmentation methods similar to those in the previous task. However, this process was applied only during training. The model architecture contains a ConvNeXt\_large backbone with a multi-head attention mechanism to capture relevant features. The network was trained using the AdamW optimizer, combined with learning rate decay, and used cross-entropy as the loss function, with class-specific weights assigned to improve the prediction of minority classes. For postprocessing, they adjusted labels based on the proportion of instances belonging to a particular category within the same localizer, improving consistency across related data points.

*5.1.2. yyama - Team Summary*

**Task 1:**

Yamagishi presented an innovative approach using MaxVit Tiny architecture for AMD progression classification between consecutive OCT scans. The preprocessing strategy uniquely mimicked clinical practice by vertically concatenating pairs of consecutive OCT images (each resized to 512x256 pixels) into a single 512x512 pixel image, effectively simulating the side-by-side comparison method used by clinicians. This fusion approach aimed to enhance the model’s ability to detect temporal changes between scans. The model architecture leveraged MaxVit Tiny’s hybrid design, combining the strengths of CNNs for local feature detection with Transformers for capturing global dependencies. Training utilized a 5-fold StratifiedGroupKFold cross-validation strategy with patient-wise grouping to prevent data leakage. The training process incorporated

comprehensive data augmentation techniques including random resized crops, horizontal flips, rotations, and coarse dropout. The model was optimized using Adam optimizer with cosine learning rate scheduling over 5 epochs. For inference, the team implemented both ensemble prediction across all 5 folds and test-time augmentation with horizontal flips.

**Task 2:**

For the three-month progression prediction task, Yamagishi developed a multimodal approach combining EfficientNet V2 S for image processing with a Multi-Layer Perceptron for handling patient metadata. The preprocessing pipeline was enhanced to include both OCT and Localizer images, concatenated vertically into a 512x512 pixel image. Patient metadata (age, gender, number of visits) was normalized and processed through a separate network branch before fusion with image features. The architecture consisted of three main components: an EfficientNet V2 S image encoder, a metadata encoder with two Dense layers, and a feature fusion classifier. The training process maintained similar augmentation and optimization strategies to Task 1, but utilized single-fold prediction with test-time augmentation for inference. The team’s implementation demonstrated how multimodal fusion of image data with patient metadata could be leveraged for long-term disease progression prediction.

*5.1.3. Cemrg - Team Summary*

**Task 1:**

They employed transfer learning by initializing MobileNetV3 with weights pretrained on ImageNet and fine-tuning it on the Task 1 dataset. To mitigate catastrophic forgetting of the pretrained features, they fine-tuned the deeper layers—containing more task-specific information—using a lower learning rate, while adapting the final layers specifically to the Task 1 data.

To address the limitations of MobileNetV3, they applied Test-Time Augmentation (TTA), generating multiple transformed versions of each image during inference. The resulting predictions were merged to enhance the model’s confidence and robustness.

They further trained five different variations of MobileNetV3 models using 5-fold cross-validation, varying initialization strategies, hyperparameters, and data augmentation techniques. This promoted diverse feature learning and resulted in a more generalized final model. The ensemble outputs were aggregated either by averaging or using a weighted sum for the final prediction.

An ablation study was performed by comparing the performance of *MobileNetV3\_base* (without ensemble

bling or TTA) against *MobileNetV3\_ensemble* (with ensembling and TTA).

**Task 2:**

The approach for Task 2 mirrored that of Task 1. They initialized MobileNetV3 with ImageNet-pretrained weights and fine-tuned it on the Task 2 dataset, carefully adjusting deeper layers at a lower learning rate to prevent catastrophic forgetting and adapting the final layers to the new task.

They again applied Test-Time Augmentation (TTA) to strengthen model robustness by merging predictions from multiple augmented versions of the input image. Five different MobileNetV3 models were trained with 5-fold cross-validation, each varying in initialization, hyperparameters, or data augmentation strategies, leading to diverse representations and a more generalized model.

Ensemble outputs were combined through averaging or a weighted sum. An ablation study comparing *MobileNetV3\_base* and *MobileNetV3\_ensemble* models was conducted to highlight the benefits of ensembling and TTA.

#### 5.1.4. *OptimaTeam - Team Summary*

**Task 1:**

SiamRETFound is a Siamese neural network designed for longitudinal change detection in retinal images. The input images are preprocessed through intensity normalization and resized to 224x224 pixels. During the training phase, data augmentation techniques such as rotation and horizontal flipping are applied to introduce variability and improve robustness. The network utilizes a large Vision Transformer architecture, initialized with pretrained weights from the RETFound model. As a pretext task, SiamRETFound is first trained on the Kermanshah dataset for a simulated *change/no-change* detection task, with labels inferred from the disease classes: if both images have the same disease, the pair is assigned to *no-change*, otherwise to *change*. It is then fine-tuned on the MARIO training dataset for target class classification. SiamRETFound employs a late fusion approach, independently extracting feature representations from each input B-scan and concatenating them for the final prediction. Ultimately, five SiamRETFound-based models are trained with variations in training settings, including different optimizers, learning rates, and augmentation schemes. In parallel, another model based on the Shifted Windows (SWIN) Transformer architecture is trained. This model integrates multiple pretext tasks, such as multi-class B-scan classification and biomarker detection as a multi-label task. Similar to SiamRETFound, the SWIN model

uses a late fusion approach for change detection. Input images are preprocessed with intensity normalization and resizing, followed by extensive data augmentation, including brightness adjustment, blurring, salt-and-pepper noise, rotation, and random eraser. To address class imbalance, the SWIN model employs the focal loss function, which assigns greater penalties to misclassified examples. SWIN models are trained using a five-fold cross-validation framework. During post-processing, predictions for a test image are obtained by averaging class probabilities across all ten models. The final classification is determined by selecting the class with the highest mean score.

**Task 2:** In Task 2, the goal is to predict the change in AMD patients within a three-months window. For pre-processing, a dataset level mean and variance are calculated to normalize the pixel values, then all images are resized to 224x224. The ViT16 model is initially pretrained with Masked Auto Encoder. In the fine-tuning step, 3-fold cross-validation is used for training 3 different models. In order to address class imbalance, focal loss is employed to put more importance to the minority classes. Additionally, the change labels are ordinal, meaning that there is an inherent ordering between the classes. a discrete Wasserstein-2 loss is added to exploit the ordinality. Finally a majority voting between these 3 models is applied to get a single prediction.

#### 5.1.5. *TONIC - Team Summary*

**Task 1:**

During the development phase, they explored four different types of models for Task 1: a baseline model and three variations. **Baseline model:** The architecture of the Baseline Model is built using two pretrained ResNet18 models that process different input data streams. The first model gets as input the images taken on  $t=0$ , the second model gets as input all the images from  $t=1$ . After training, the outcome features from both models are then combined and fed into a new fully connected layer that makes the final classification. **Extra Layer:** To improve the model, they added an extra layer to the baseline model after combining the two ResNet models. They expect that this will improve the model because this extra layer could make connections between the two models and learn from the feature interaction. **Balanced Batches:** To optimize our model in a different way, they focus on the unequal distribution of classes detailed in Section 2.1. To make sure that the model learns about every class equally, They train a model with balanced batches: ensuring that each batch of data used during training contains an equal or proportionate number of samples from each class. Balanced

batches are achieved by iterating through separate data loaders for each class. During each iteration, a batch is drawn from each loader, and then the samples are concatenated together to form a single batch that contains an equal number of samples from each class. This approach helps the model to learn equally from all classes, preventing it from becoming biased towards the more frequent ‘stable’ class. **Balanced Batches and Augmented Data:** Some data augmentation was applied to artificially expand the diversity of the training dataset by applying various transformations. Data augmentation was implemented through a series of image transformations, including random horizontal and vertical flips, rotations, brightness/contrast (with PyTorch ColorJitter), and resized cropping. The datasets are then combined to create a comprehensive training set that includes both the original and augmented images. They combine this method with our balanced batches approach. For Task 1, they generate 15,000 samples per class. Thus, they end up with a dataset that is four times as big as the original dataset of which the classes are balanced.

#### **Task 2:**

Task two has similar approaches as Task 1. First, the baseline model is a pre-trained ResNet18 model that was trained on 70% of the training data. Second, the same model is retrained with balanced batches, to exclude the effect of the class distribution; similar to Task 1. Lastly, the balanced batches model was extended with augmented data by *torchvision.transforms*; also similar to Task 1.

#### 5.1.6. FERLIV - Team Summary

##### **Task 1:**

The FERLIV team proposed a modular, fully transformer-based approach for monitoring the progression of wet AMD using two registered OCT B-scans from two consecutive medical exams. The method consists of three transformer encoder architectures: Feature Encoder, Change Encoder, and Diagnosis Encoder. The Feature Encoder is the first part of the method, where a large Vision Transformer Kolesnikov et al. (2021) encodes a pair of OCT B-scans into two sets of local feature vectors. The Change Encoder detects visual changes in a retina using a dual Multi-Change Captioning Transformer Qiu et al. (2021) with a co-attention mechanism Lu et al. (2019). The outputs of the Change Encoder are concatenated based on their corresponding 2D positions and forwarded to the third and final transformer encoder, i.e., the Diagnosis Encoder, which quantifies changes in disease progression. The Diagnosis Encoder uses a self-attention mechanism and is

followed by the classification head. During preprocessing, OCT B-scans are resized and cropped to  $224 \times 224$  pixels, followed by normalization. Before training, the Feature Encoder is initialized with weights from the pretext task, where RETFound’s ViT-Large model Zhou et al. (2023) is used as a Segmenter encoder Strudel et al. (2021) for the segmentation of retinal layers on the OCT MS and Healthy Control dataset He et al. (2019). This public dataset is acquired on the same device as the MARIO dataset, addressing variability caused by inter-device transfer. Pretext task results in improved performance for Task 1, as changes in retinal structures are crucial for monitoring disease progression. All three encoders are trained using the AdamW optimizer with cosine learning rate scheduling and weight decay. A weighted categorical cross-entropy loss function is used to address the class imbalance. Augmentation techniques include random resized cropping and random horizontal flipping to improve generalization.

##### **Task 2:**

For Task 2, the FERLIV team utilizes the modular approach from Task 1, modifying the three-part method by removing the middle component, i.e., the Change Encoder, from the pipeline. The Feature Encoder and Diagnosis Encoder are initialized with weights from Task 1, enabling knowledge transfer from the simpler task to the more challenging one. In Task 2, the Feature Encoder extracts local feature vectors from a single OCT B-scan, while the Diagnosis Encoder is followed by a new classification head. Preprocessing, augmentation techniques, and most training details remain the same as in Task 1. To better address the more apparent class imbalance in Task 2, weighted random sampling is introduced in addition to the weighted categorical cross-entropy loss function.

#### 5.1.7. MIPLAB Team Summary

##### **Task 1:**

Our approach for Task 1 integrates all available data modalities, including OCT B-scans, infrared localizer images, and clinical variables, to classify changes in neovascular activity between two consecutive time points. They begin by preprocessing the image data (resizing OCT B-scans to  $496 \times 496$  pixels and infrared localizer images to  $384 \times 384$  pixels) and standardizing clinical variables using z-score normalization (subtracting the mean and dividing by the standard deviation). They finetune RETFound (a ViT-large based foundation model) and EfficientNetV2 on the MARIO training set using cross-entropy loss, and then use these finetuned models to extract feature representations from the imaging data. These representations are combined with the

patient’s clinical data to create a unified feature vector for each patient on a slice-by-slice basis. To incorporate volumetric context, global average pooled features of all B-scans within a 3D OCT C-scan are also added to the feature vectors. Principal component analysis (PCA) is used to reduce the dimensionality of the feature space and to mitigate the risk of overfitting. A support vector classification (SVC) model with hinge loss serves as the final classifier. Random data augmentations (horizontal and vertical flips, rotations, translations, and contrast adjustments) are employed to enhance model generalizability. They further employ a semi-supervised strategy by assigning pseudo labels to unlabeled validation data, which had a prediction probability above a pre-specified confidence threshold. The SVC model is then retrained on this enriched dataset.

**Task 2:**

For Task 2, They utilize all available data modalities, including OCT B-scans, infrared localizer images, and clinical variables, to predict three-month progression in neovascular activity from a single time point. The image data is preprocessed by resizing OCT B-scans to 496×496 pixels and infrared localizer images to 384×384 pixels. Clinical variables undergo standardization using z-score normalization (subtracting the mean and dividing by the standard deviation). They finetune RETFound and EfficientNetV2 on the MARIO training set using cross-entropy loss, and subsequently utilize these models to extract feature representations from the imaging data. These representations are combined with the patient’s clinical data to create a unified feature vector for each patient on a slice-by-slice basis. To incorporate volumetric context, global average pooled features from all B-scans within a 3D OCT C-scan are added to the feature vectors. PCA is employed to reduce the dimensionality of the feature space and mitigate the risk of overfitting. An ordinal logistic classification model with an immediate-threshold loss variant is trained to directly predict graded progression outcomes. To improve model generalizability, random data augmentations were applied, including horizontal and vertical flips, rotations, translations, and contrast adjustments.

*5.1.8. MIC Group 6 - Team Summary*

**Task 1:**

In this study, a robust framework was developed to classify changes in AMD progression between two time-point OCT scans. The architecture centered on a Siamese network, specifically designed to harness the temporal information encoded in paired OCT scans. Preprocessing steps included intensity normalization,

resizing all images to a standardized resolution, and ensuring precise anatomical alignment between scans for consistency. Extensive experimentation revealed that the best-performing approach for Task 1 utilized a Siamese network with the ImageNet encoder. This encoder efficiently extracted feature representations from both time points, which were subsequently combined through element-wise subtraction to emphasize temporal changes. The resulting feature vector was fed into fully connected classification layers to predict progression states (reduced, increased, stable, or uninterpretable).

**Task 2:** A novel hybrid framework was designed to predict AMD progression from a single OCT scan, building upon the findings from Task 1. The preprocessing pipeline mirrored that of Task 1, ensuring consistency across both tasks. Additionally, the fine-tuned encoder from Task 1 was adapted for use in Task 2. Although extensive evaluation on more complex models was performed, the Siamese Network with ImageNet encoder emerged as the top-performing model. It demonstrated superior capability in extracting detailed features from single scans, making it well-suited for capturing subtle disease-specific patterns necessary for accurate progression prediction.

*5.1.9. STEP - Team Summary*

**Task 1:** The STEP team developed a novel deep learning model, designed to classify the evolution between consecutive OCT B-scans, using contextual information from adjacent B-scans part of an OCT volume and at two time instants. The preprocessing workflow involved constructing OCT volumes from grouped B-scans, applying intensity normalization using computed mean and standard deviation, and resizing each B-scan to a fixed size of 224x224 pixels for consistency. To address dataset variability, the team implemented targeted data augmentation using the MONAI framework during training, applying random flip in all dimensions, random intensity scaling and random Gaussian noise addition to enhance robustness against overfitting. For imbalanced classes, volume-level augmentation was carefully synchronized across paired scans. The STEP team’s architecture combined a pretrained vision transformer (ViT) backbone, RETFound, with a bidirectional cross-attention module designed to capture dependencies between sequential B-scan pairs. CLS tokens extracted from the B-scans were processed to compute temporal relationships, with cross-attention improving the model’s sensitivity to subtle changes in progression. A linear layer generated individual predictions for each B-scan. The training pipeline employed the AdamW

optimizer with a weight decay of 0.05 with cosine learning rate scheduling and 10 warm-up epochs to ensure smooth convergence. Evaluation metrics guided model selection, with predictions aggregated using batched inference for OCT volumes. Post-processing involved assigning predictions slice-by-slice, leveraging the context learned by the model. This approach demonstrated consistent classification improvements across metrics, highlighting the efficacy of integrating sequential context and advanced transformer-based methods.

**Task 2:** For Task 2, the STEP team designed a specialized Multiple Instance Learning (MIL)-based architecture to identify the most significant slices within an OCT volume to predict disease progression within a 3-month period. The preprocessing pipeline involved constructing fixed-size OCT volumes (25 B-scans each) by selecting central slices and replicating boundary slices for smaller volumes. Intensity normalization was applied based on mean and standard deviation, ensuring consistent input data. To address variability, targeted data augmentation was employed using the MONAI framework, incorporating random flip in all dimensions, random intensity scaling and random Gaussian noise addition transformations. The proposed solution utilized a vision transformer (ViT) backbone, RETFound, pre-trained on retinal imaging tasks. This backbone extracted feature vectors from each B-scan, which were then processed by a MIL attention module. The attention mechanism assigned importance scores to slices within the volume, highlighting regions with critical biomarkers such as retinal fluid. A final linear layer aggregated these features to predict progression of activity for the entire volume. The training process used the AdamW optimizer with a weight decay of 0.05, cosine learning rate scheduling and class-weighted sampling to counter data imbalance. During inference, predictions were made at the volume level, with results extended to the original B-scans.

#### 5.1.10. DF41 - Team Summary

##### **Task 1:**

For Task 1, the DF41 team used a Late Fusion CNN architecture to classify progression changes between two consecutive retinal OCT scans. The preprocessing pipeline leveraged the OCT image segmentation library Optical Coherence Tomography Image Preprocessing (OCTIP). Two segmentation models, FPN-EfficientNet-B6 and FPN-EfficientNet-B7, were employed to generate segmentation masks. The median of the outputs from these models was applied to ensure robust predictions. Once the segmented regions were extracted, the upper boundary of the retina (inner limiting mem-

brane) was aligned with the top of the image, effectively "flattening" the retina and realigning the scans along the depth axis. This preprocessing step is crucial for improving analysis quality and enhancing classification performance by eliminating noise and irrelevant information. The output of this step was an image with dimensions of  $512 \times 200$  pixels. Next, the Late Fusion CNN network employed the ResNet50 architecture to extract two feature maps of size 2048 from the paired OCT images without resizing, ensuring that no information was lost. These feature maps were concatenated into a single map of size 4096, which was then passed through a fully connected layer to produce the classification output. To enhance the diversity of the training dataset and improve model robustness, various data augmentation techniques were applied, including RandomHorizontalFlip, RandomVerticalFlip, RandomRotation, ColorJitter, RandomPerspective, and GaussianBlur. To address class imbalance and further boost performance, an ensemble method was used. Four models were trained through cross-validation, and the predictions from all models were averaged during post-processing. These combined strategies contributed to strong performance in classifying the progression between two consecutive OCT slices. In particular, OCTIP showed improved performance with enhanced F1 scores and rank correlation.

##### **Task 2:**

For Task 2, DF41 introduced a novel method called Patch Progression Masked Autoencoder (PPMAE), which predicts a future OCT image based on the current scan, utilizing the dataset from Task 1. They approach this task by reconstructing the future state of the current image and then performing disease progression classification. The PPMAE model works by masking 75% of the current OCT image at time  $t_0$  and predicting the corresponding patches from the  $t_1$  image, allowing the model to capture temporal changes and disease progression between the patches. After predicting the future patches, they are aligned with the unmasked regions of the  $t_0$  image, resulting in a reconstructed future OCT image that corresponds to the image several months later. During training, RandomResizedCrop and RandomHorizontalFlip augmentations were applied, and the reconstruction error was evaluated using Mean Squared Error (MSE) between the predicted and actual patches at  $t_0$ . OCTIP preprocessing was also used for this reconstruction task, improving the quality of the image reconstruction. Finally, the model from Task 1 was re-trained to predict AMD progression by using both the current OCT image and the predicted future image.

### 5.1.11. *scyyd4 - Team Summary*

**Task 1:** The scyyd4 team proposed a novel AI framework, OCT-DiffNet, designed for detecting neovascular activity in Age-related Macular Degeneration (AMD) using sequential OCT images. The preprocessing pipeline included cropping, resizing each image to  $224 \times 224$  pixels, and intensity normalization to enhance the input consistency. To further augment the training data and improve model generalization, the team employed targeted data augmentation techniques, such as random rotations, zoom, and brightness adjustments, simulating realistic variations in the OCT imaging process. OCT-DiffNet is built upon a modified ConvNeXt V2-Large architecture, which was fine-tuned for this task. The model processes pairs of consecutive OCT images and computes temporal differences using a Siamese network structure. Key architectural modifications included adjusting the first convolutional layer to accommodate single-channel (grayscale) OCT images and introducing custom fully connected (FC) layers to analyze the extracted features and their differences. These enhancements allow the model to effectively capture subtle changes indicative of disease progression. The training pipeline utilized a cross-entropy loss function, optimized with the Adam optimizer. To further boost prediction accuracy and robustness, an ensemble method was employed, combining predictions from five models trained with 5-fold cross-validation. Post-processing involved majority voting across the ensemble predictions, ensuring stable and reliable outputs. The proposed method achieved significant improvements in performance metrics, demonstrating its potential for precise AMD progression detection and clinical applicability.

**Task 2:** The scyyd4 team presented an innovative solution for predicting disease progression in Age-related Macular Degeneration (AMD) over a three-month period, leveraging a multi-instance learning framework, CLAM-SB, combined with the ConvNeXt V2 feature extractor. Preprocessing steps included converting OCT images to grayscale, resizing them to  $224 \times 224$  pixels, and normalizing pixel intensities based on dataset-specific mean and standard deviation values to enhance consistency. A weighted random sampler was employed to address the class imbalance, ensuring proportional representation of each class during training. The core architecture utilized ConvNeXt V2 as a frozen feature extractor to generate robust image embeddings, which were fed into the CLAM-SB model. This multi-instance learning approach aggregated features across multiple OCT scans (bags), enabling the model to cap-

ture nuanced patterns indicative of disease progression. Custom fully connected layers within the CLAM-SB framework were optimized to classify cases into three progression categories: no progression, mild progression, and significant progression. Additionally, a gated attention mechanism in CLAM-SB highlighted the most relevant instances within each bag, improving interpretability and prediction accuracy. The training pipeline employed a weighted cross-entropy loss function to handle class imbalance and was optimized using the Adam optimizer with a learning rate scheduler. Dropout regularization was excluded to preserve model capacity, while data augmentation was omitted following preliminary experiments that revealed augmentation-induced instability. The final model ensemble was built using predictions from five models trained with different random seeds, ensuring stable and reliable outputs. Post-processing involved majority voting across bags, enhancing prediction consistency at the patient level.

### 5.1.12. *jkulinzstudents - Team Summary*

**Task 1:** This work proposes a ViT-based deep learning approach to classify progression changes between consecutive retinal OCT B-scans. The preprocessing pipeline includes resizing all images to  $224 \times 224$  pixels and intensity normalization to enhance feature consistency. Data augmentation techniques, such as random flipping, zooming, cropping, rotation, and noise injection, are applied to improve robustness. The method employs a pretrained DinoV2 ViT model with registers to extract feature embeddings from each B-scan. These features are concatenated and passed through a two-layer MLP to generate classification predictions for disease progression. A 10-fold cross-validation strategy ensures reliable performance by varying stratification seeds to create diverse patient splits. The final prediction is obtained by aggregating softmax scores across all folds. This approach effectively captures subtle changes in neovascular activity and demonstrates strong performance in classification metrics.

**Task 2:** The jkulinzstudents team employed a two-step deep learning approach to predict disease progression over a 90-day period using a single OCT B-scan. The preprocessing pipeline involved resizing each OCT scan to  $224 \times 224$  pixels, aligning with the input requirements of our feature extraction backbone, RETFound. The images were then normalized using standard ImageNet statistics to ensure consistency across the dataset.

Our approach was divided into two stages: Latent Matching and Disease Progression Classification. In the first stage, the Latent Matching model estimated the fu-

ture state of the disease by predicting the embedding of the OCT scan at  $t_{90}$ , leveraging the frozen feature extractor of RETFound. This step used a three-layer MLP trained with negative cosine similarity loss, ensuring that the predicted embedding closely aligned with the true future representation. The Adam optimizer was employed with an initial learning rate of  $1e^{-3}$ , reduced adaptively when training plateaued.

In the second stage, the Disease Progression Classification model utilized the embeddings from  $t_0$  and the predicted embeddings at  $t_{90}$  to classify the disease progression into three categories: Reduced, Stable, or Increased activity. The concatenated embeddings were passed through another three-layer MLP, optimized with cross-entropy loss. This stage was trained using the available dataset from Task 1 to ensure sufficient data coverage for all progression classes.

To further improve performance, They experimented with fine-tuning the RETFound model on the provided OCT images using a masked image modeling approach. However, as this did not yield significant performance improvements, They opted to retain the original pre-trained RETFound model to avoid overfitting.

Post-processing was minimal, with the only adjustment being the reassignment of the Uninterpretable category to Stable, due to class imbalances. While effective for competition purposes, Theynote that uninterpretable predictions should ideally be flagged for further medical review.

## 6. Results

### 6.1. Evaluation Metrics and Ranking Methodology

This section details the evaluation framework and presents the final rankings for the twelve competition finalists. The ranking system was meticulously developed prior to the challenge to ensure an objective assessment of submissions, while reflecting the relative importance and complexity of each task.

Given the distinct challenges associated with the two tasks, a specific weighting scheme was implemented to prioritize clinical relevance and task difficulty. In particular, Task 2 was assigned twice the weight of Task 1 in the final ranking calculation.

#### 6.1.1. Task-specific Scoring Formulas

Participant performance on each task was evaluated based on a weighted combination of multiple metrics, as described below.

*Task 1: Structural Classification Score.* Task 1 involved the classification of consecutive two-dimensional optical coherence tomography (OCT) B-scan slices. The task’s score,  $f_{\text{task}_1}$ , was computed as:

$$\begin{aligned} f_{\text{task}_1} = & 0.5 \times \text{F1-score} \\ & + 0.25 \times \text{Rank-correlation} \\ & + 0.25 \times \text{Specificity} \end{aligned} \quad (1)$$

*Task 2: Disease Progression Prediction Score.* Task 2 focused on predicting the evolution of age-related macular degeneration (AMD) over a three-month period. The corresponding score,  $f_{\text{task}_2}$ , was calculated as:

$$\begin{aligned} f_{\text{task}_2} = & 0.1 \times \text{F1-score} \\ & + 0.2 \times \text{Rank-correlation} \\ & + 0.1 \times \text{Specificity} \\ & + 0.6 \times \text{Quadratic Weighted Kappa} \end{aligned} \quad (2)$$

#### 6.1.2. Final Ranking Computation

The overall ranking score was obtained by combining the two task-specific scores using a weighted average:

$$\text{Final Score} = 0.35 \times f_{\text{task}_1} + 0.65 \times f_{\text{task}_2} \quad (3)$$

This formulation reflects the higher clinical relevance and predictive difficulty associated with Task 2.

### 6.2. Rationale for Metric Weighting

The metric weighting scheme was designed to balance predictive performance with clinical importance, taking into account the specific objectives and challenges of each task:

- **Task 1 – Structural Classification:** This task targeted the classification of local structural changes observable in consecutive 2D OCT slices. Although essential for characterizing retinal morphology, it primarily addresses short-term variations and was considered comparatively less complex. Consequently, the F1-score, which balances precision and recall, was assigned the highest weight (50%), while Rank Correlation and Specificity were equally weighted (25% each) to capture ordinal consistency and specificity in classification.

- **Task 2 – Disease Progression Prediction:** Task 2 required forecasting AMD progression over a three-month interval, posing a significantly higher clinical and modeling challenge. The Quadratic Weighted Kappa, a robust metric for ordinal classification agreement, was therefore assigned the largest weight (60%). Additional contributions from the F1-score, Rank Correlation, and Specificity ensured a comprehensive evaluation across multiple performance dimensions.

### 6.3. Dataset from Brest

The rankings of various teams based on their performance on the Brest dataset for Task 1 and Task 2 are summarized in Tables 5 and 6, respectively. The overall ranking based on both tasks is presented in Table 7.

#### 6.3.1. Task 1

Figure 8 presents the misclassification matrix for Task 1, showing the frequency of errors across various patients in the Brest dataset.

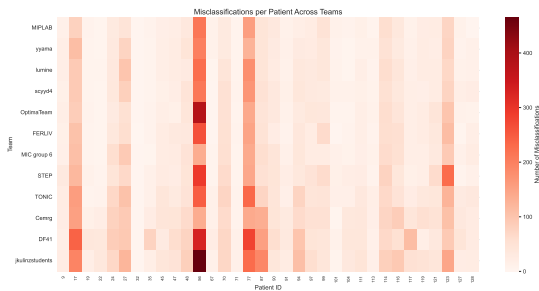


Figure 8: Misclassification matrix for Task 1 showing the frequency of errors across various patients in the Brest dataset.

To further evaluate the classification performance, Figure 9 illustrates the confusion matrix for Task 1, highlighting the model’s performance across all classes.

To analyze the effect of temporal differences on accuracy, Figure 10 presents a heatmap of accuracy over delta time for Task 1.

Figure 11 provides a visualization of the model’s performance based on the number of visits, showcasing the differences in accuracy across varying patient visit distributions.

#### 6.3.2. Task 2

For Task 2, Figure 12 displays the misclassification matrix, which outlines the distribution of errors across different patients.

To complement this analysis, Figure 13 presents the confusion matrix for Task 2, offering detailed insights into the classification accuracy per class.

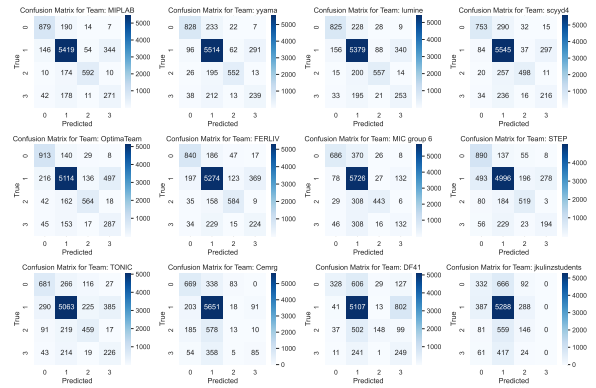


Figure 9: Confusion matrix for Task 1 highlighting the performance of the model across all classes in the Brest dataset. Correct classifications and misclassifications are shown for each class.

#### 6.3.3. Ranking on the test set from Brest

Table 5: Ranking for task 1 of the test set of the Brest dataset.

Team	F1 score	Rk-correlation	Specificity	final score task1
MIPLAB	0.858	0.692	0.922	0.833
yyama	0.855	0.676	0.914	0.825
lumine	0.840	0.652	0.911	0.811
scyyd4	0.840	0.635	0.899	0.804
OptimaTeam	0.824	0.645	0.919	0.803
FERLIV	0.829	0.637	0.911	0.802
MIC group 6	0.837	0.613	0.884	0.793
STEP	0.791	0.576	0.902	0.765
TONIC	0.770	0.518	0.886	0.736
Cemrg	0.769	0.425	0.844	0.702
DF41	0.699	0.308	0.820	0.632
jkulinzstudents	0.691	0.211	0.795	0.597

Table 6: Ranking for task 2 of the test set of the Brest dataset.

Team	F1 score	Rk-correlation	Specificity	Quadratic-weighted Kappa	final score task2
MIPLAB	0.822	0.187	0.710	0.192	0.306
DF41	0.822	0.210	0.723	0.154	0.289
MIC group 6	0.749	0.205	0.809	0.122	0.270
scyyd4	0.766	0.063	0.681	0.111	0.224
STEP	0.739	0.035	0.671	0.118	0.219
Cemrg	0.803	0.066	0.679	0.093	0.217
FERLIV	0.634	0.108	0.712	0.099	0.216
jkulinzstudents	0.661	0.107	0.711	0.087	0.211
TONIC	0.811	0.071	0.682	0.058	0.198
yyama	0.809	0.018	0.666	0.073	0.195
lumine	0.730	0.029	0.672	0.077	0.192
OptimaTeam	0.730	0.087	0.706	0	0.158

### 6.4. Dataset from Tlemcen

The dataset from Tlemcen provides a unique opportunity to evaluate model generalization on a different population. Tables 8 and 9 summarize the rankings for Task 1 and Task 2, respectively, while the final overall rankings are given in Table 10.

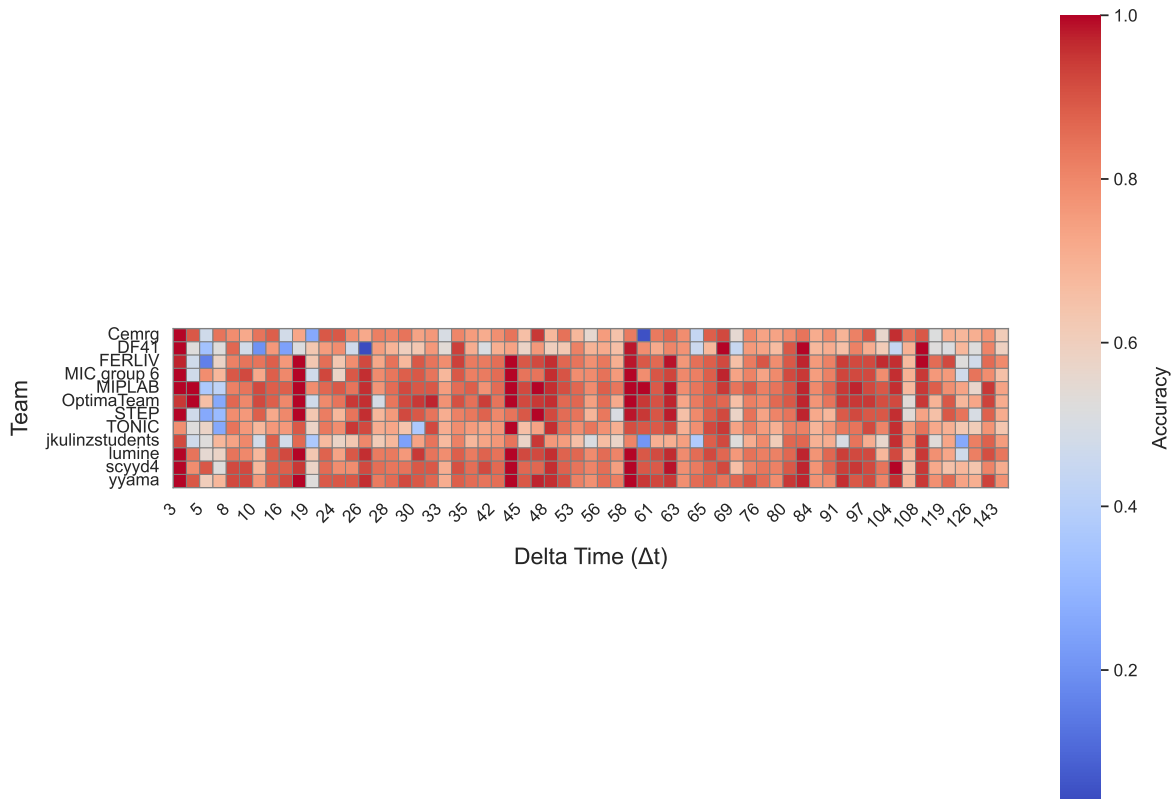


Figure 10: Heatmap of accuracy over delta time for Task 1 in the Brest dataset. This visualization reveals how accuracy varies with respect to time differences, offering a temporal performance analysis.

Table 7: Final ranking on the test set of the Brest dataset.

Team	final score task2	final score task1	overall ranking
MIPLAB	0.306	0.833	0.490
MIC group 6	0.270	0.793	0.453
scyyd4	0.224	0.804	0.427
FERLIV	0.216	0.802	0.421
yyama	0.195	0.825	0.415
STEP	0.219	0.765	0.410
DF41	0.289	0.632	0.409
lumine	0.192	0.811	0.409
Cemrg	0.217	0.702	0.387
TONIC	0.198	0.736	0.386
OptimaTeam	0.158	0.803	0.384
jkulinzstudents	0.211	0.597	0.346

This special edition of MICCAI marks a significant milestone as the first to be held on the African continent, emphasizing the importance of regional diversity in advancing medical imaging and computational research. A key aspect of this event was the opportunity

for participants to evaluate their algorithms on an unseen dataset, distinct from the one provided during the training phase. This experimental setup allowed for a rigorous assessment of model performance under real-world conditions, particularly in the context of domain adaptation and generalizability.

The dataset, sourced from Algeria, was specifically designed to study algorithmic performance in the presence of *device shift*—variations in imaging equipment and acquisition protocols—as well as *population shift*, where demographic and physiological characteristics differ from those in the training cohort. These factors are crucial in medical AI research, as they directly influence model robustness and the fairness of automated diagnostic tools across diverse clinical settings. Addressing these challenges remains a strong focus of the MICCAI community, aligning with global efforts to develop AI-driven healthcare solutions that are both reliable and equitable.

The Algerian dataset comprises **five patients** undergoing **long-term treatment for age-related macular**

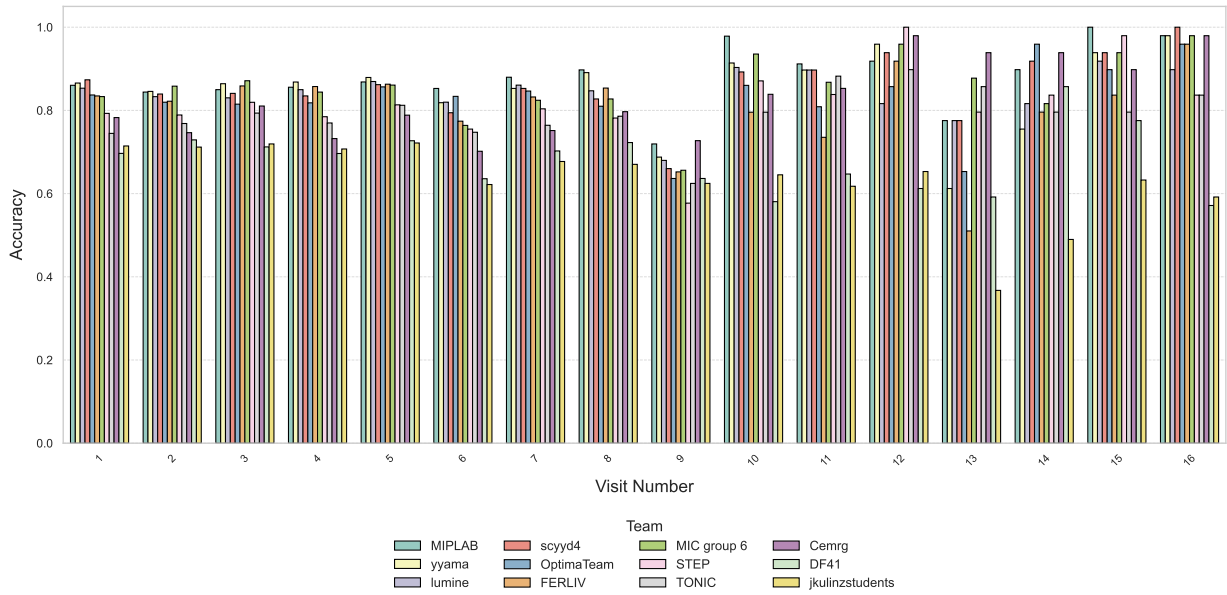


Figure 11: Representation of the performance of each team for the different numbers of visits observed within the patient distribution.

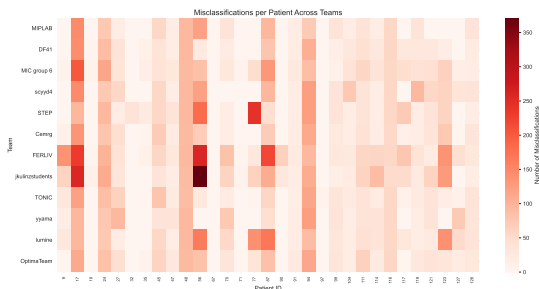


Figure 12: Misclassification matrix for Task 2 illustrating the distribution of errors across different patients for the Brest dataset.

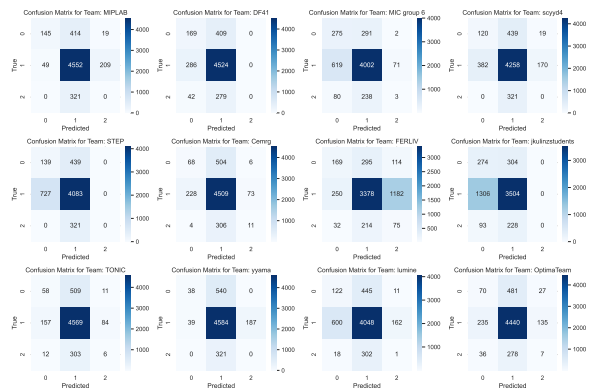


Figure 13: Confusion matrix for Task 2 displaying the model's classification performance per class in the Brest dataset. It provides detailed insights into the accuracy of Task 2 predictions.

**degeneration (AMD) in Algeria.** For analysis at the **B-scan level**, **Task 1** includes **703 cases**, while **Task 2** consists of **574 cases**, ensuring adherence to the same constraints and experimental conditions established in the original challenge.

To ensure **consistency, fairness, and reliability** in performance evaluation, the **same ranking methodology** used for the original dataset was applied to the Algerian dataset. This comparative analysis provides **valuable insights** into the adaptability of different models across diverse populations, highlighting their **strengths, limitations, and potential areas for improvement** in medical AI applications.

#### 6.4.1. Task 1

Figure 15 presents the misclassification matrix for Task 1, showing the frequency of errors across various classes in the dataset from Tlemcen. This visualization helps in identifying specific patterns of misclassification.

As illustrated in Fig. 14, the heatmap systematically characterizes the evolution of predictive accuracy as a function of the time interval (delta time) for Task 1 using the Tlemcen dataset. The color gradient from dark (lower accuracy) to bright (higher accuracy) enables an

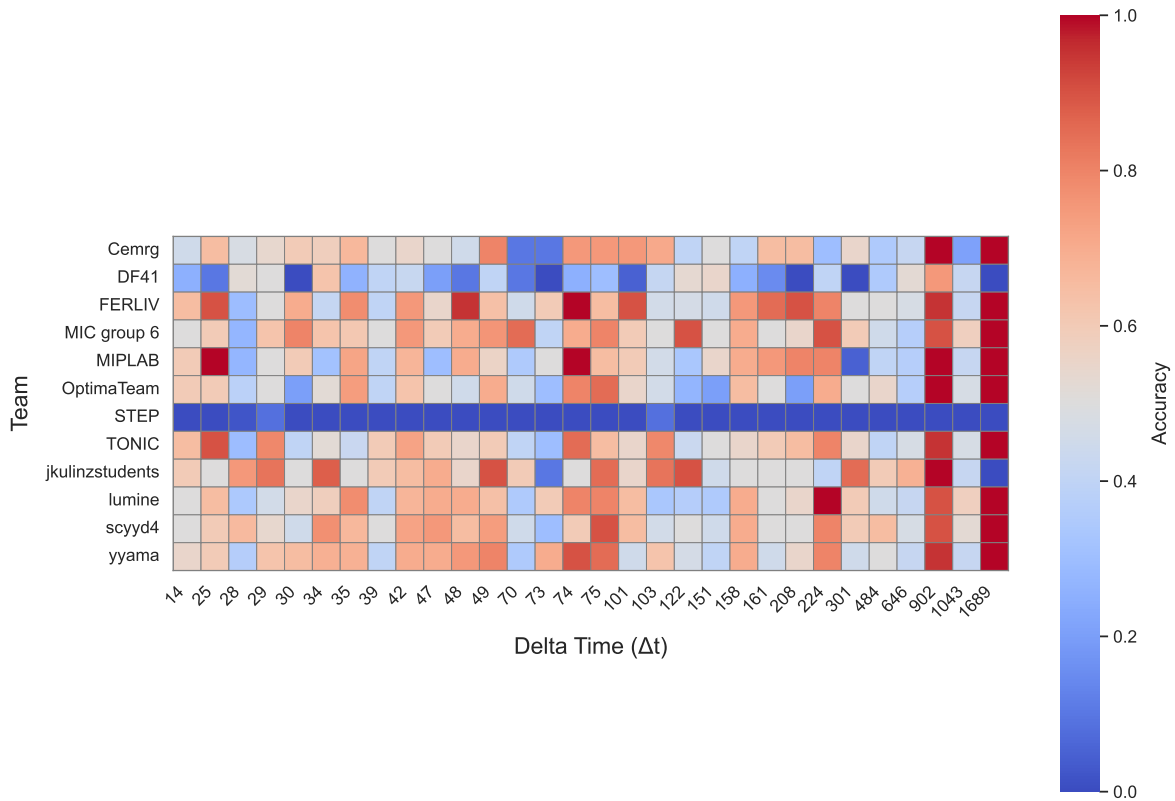


Figure 14: Heatmap of accuracy as a function of delta time for Task 1 on the Tlemcen dataset. The horizontal axis represents the delta time ( $t_t$ ) between baseline and follow-up scans, while the vertical axis lists the competing teams. Color intensity corresponds to the accuracy, with brighter areas indicating higher predictive performance. This visualization provides an in-depth temporal analysis of model generalization across varying time intervals.

immediate visual comparison across different teams and time horizons.

A detailed inspection reveals significant performance heterogeneity among the participating teams. Notably, the STEP team consistently underperforms across all delta time intervals, achieving considerably lower accuracy compared to other teams, regardless of the prediction horizon. This systematic underperformance can be attributed to methodological differences: specifically, the STEP team’s approach incorporates a hyperparameter fine-tuned on OCT volumes from the Brest dataset. The Brest dataset features complete volumetric acquisitions, with specific slice distributions and characteristics that differ substantially from the Tlemcen dataset.

In contrast, the Tlemcen dataset is composed of B-scan sequences that do not fully reconstruct a volumetric OCT scan, and the number of available B-scans per case differs significantly from the Brest data distribution. As a result, the STEP model faces a domain shift, encountering input data that violate the assumptions un-

derlying its optimized configuration. This mismatch explains the degradation in performance observed across all temporal spans.

Furthermore, Fig. 14 suggests that some teams demonstrate relative robustness to variations in delta time, while others are more sensitive. Such trends underline the importance of model adaptability and the need for transfer learning strategies or domain generalization techniques to ensure reliable longitudinal prediction across datasets with different acquisition protocols and distributions.

To further analyze classification performance, Figure 16 shows the confusion matrix for Task 1, highlighting the model’s accuracy across all classes.

#### 6.4.2. Task 2

For Task 2, Figure 17 displays the misclassification matrix, illustrating the distribution of errors across different classes. This helps in identifying which classes are most frequently misclassified.

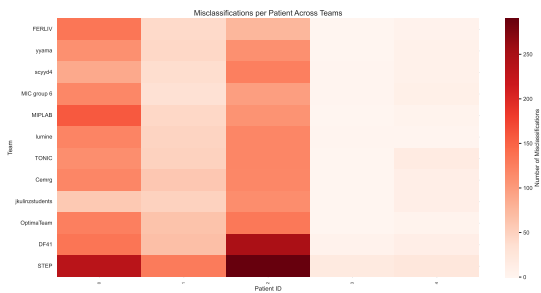


Figure 15: Misclassification matrix for Task 1 showing the frequency of errors across various classes in the dataset from Tlemcen. This helps identify patterns of misclassification specific to Task 1.

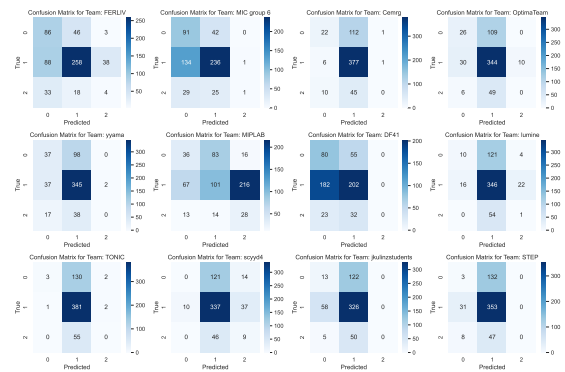


Figure 18: Confusion matrix for Task 2 displaying the model's classification performance per class in the Tlemcen dataset. It provides detailed insights into the accuracy of Task 2 predictions.

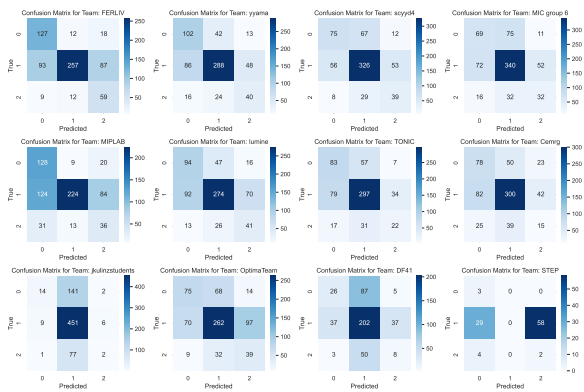


Figure 16: Confusion matrix for Task 1 highlighting the performance of the model across all classes in the Tlemcen dataset. Correct classifications and misclassifications are shown for each class.

Table 8: Presentation of the task1 ranking obtained on the dataset from Tlemcen.

team	F1_score	Rk-correlation	Specificity	final score Task 1
FERLIV	0.630	0.458	0.876	0.648
yyama	0.612	0.349	0.844	0.604
MIC group 6	0.627	0.274	0.820	0.587
scyyd4	0.626	0.312	0.830	0.598
lumine	0.582	0.302	0.830	0.574
TONIC	0.572	0.256	0.820	0.555
Cemrg	0.562	0.194	0.804	0.531
jkulinzstudents	0.664	0.113	0.683	0.531
MIPLAB	0.552	0.358	0.852	0.579
OptimaTeam	0.535	0.213	0.801	0.521
DF41	0.336	-0.023	0.732	0.345
STEP	0.007	-0.040	0.746	0.180

Table 9: Presentation of the task2 ranking obtained on the dataset from Tlemcen.

Team	F1 score	Rk-correlation	Specificity	Quadratic-weighted Kappa	Final Ranks Task 2
MIPLAB	0.287	-0.062	0.620	0.182	0.187
FERLIV	0.606	0.268	0.770	0.158	0.286
MIC group 6	0.571	0.225	0.812	0.126	0.259
OptimaTeam	0.645	0.098	0.689	0.103	0.215
DF41	0.491	0.076	0.692	0.087	0.186
yyama	0.666	0.184	0.719	0.059	0.211
lumine	0.622	-0.001	0.664	0.059	0.164
Cemrg	0.695	0.226	0.711	0.054	0.218
scyyd4	0.603	0.004	0.667	0.014	0.136
TONIC	0.669	0.060	0.672	0.010	0.152
jkulinzstudents	0.591	-0.063	0.650	-0.021	0.099
STEP	0.620	-0.066	0.656	-0.099	0.055

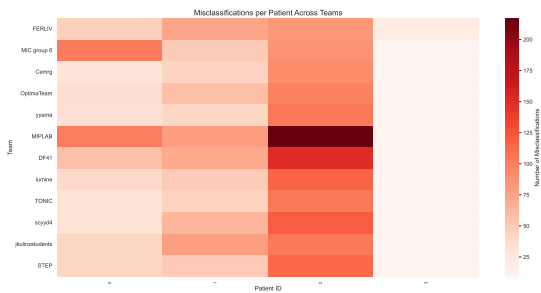


Figure 17: Misclassification matrix for Task 2 illustrating the distribution of errors across different classes for the Tlemcen dataset. This provides insight into which classes are commonly misclassified.

Table 10: Presentation of the final ranking obtained on the dataset from Tlemcen.

Team	final score 2	final score 1	Overall ranking
FERLIV	0.286	0.648	0.413
MIC group 6	0.259	0.587	0.374
yyama	0.211	0.604	0.348
Cemrg	0.218	0.531	0.328
MIPLAB	0.187	0.579	0.324
OptimaTeam	0.215	0.521	0.322
lumine	0.164	0.574	0.307
scyyd4	0.136	0.598	0.298
TONIC	0.152	0.555	0.293
jkulinzstudents	0.099	0.531	0.250
DF41	0.186	0.345	0.242
STEP	0.055	0.180	0.099

To complement this analysis, Figure 18 presents the confusion matrix for Task 2, offering a detailed breakdown of classification performance across different classes.

### 6.4.3. Ranking on the test set from Algeria

### 6.5. Correlation results between the two datasets.

We observe the same trend in terms of difficulties for task 1 and task 2 for both datasets. We observe a clear drop of performance for task 1, while for task 2 the results are still low but reside in the range of the Brest dataset. Interestingly, we observe that one of the team (jkulinzstudents) that was considered to be ranked as the lowest in the Brest dataset for task 2, is now considered to be the best method in terms of F1 score and Kappa score. Their approach focuses on the pre-training stage that consisted in being able to create the next scan using the B-scan at time  $t$  do generate the B-scan at time  $t + 1$ . In this section, we analyze the correlation between the results obtained on the Brest and dataset from Tlemcens. The goal is to assess the consistency of model performance across different datasets, particularly in the presence of population and device shifts.

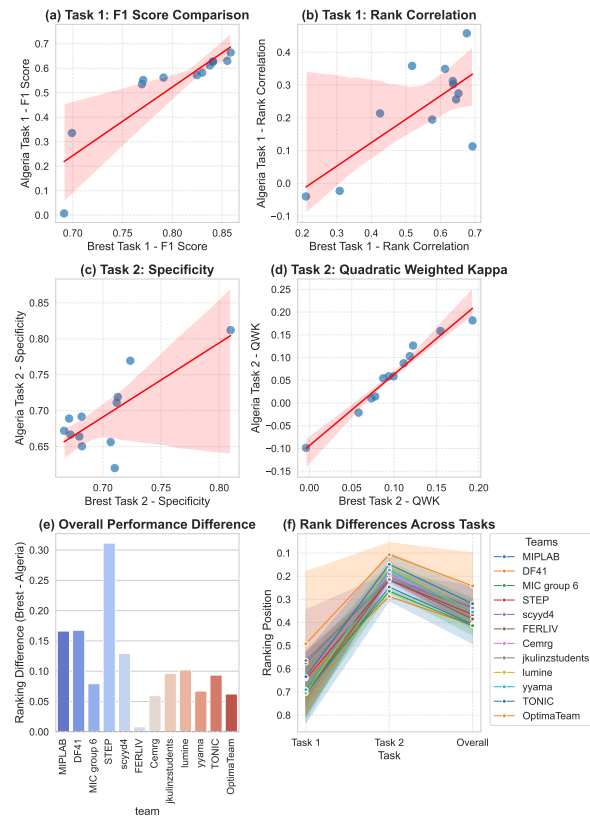


Figure 19: Comparative analysis of Brest and Algeria rankings across different tasks. (a)-(d) present scatter plots for individual task metrics, (e) shows overall ranking differences, and (f) provides a ranking evolution plot across tasks.

To determine the relationship between the performance on the Brest and Tlemcens datasets, we analyze

the final rankings across both datasets. Figure 19 illustrates the correlation between the overall rankings from both datasets.

Fig. 19 presents a comparative analysis of team rankings across the Brest and Tlemcens datasets, highlighting performance variations in different tasks. Each subplot illustrates a key evaluation metric, providing insight into ranking stability and dataset-dependent effects.

Fig. 19 (a) compares F1 scores for Task 1. The scatter plot indicates a moderate relationship between scores across datasets, suggesting that while some teams perform consistently, others exhibit dataset-specific variations. Fig. 19 (b) shows the rank correlation for Task 1, where weaker correlations imply differences in ranking distributions, reflecting potential shifts in dataset composition or model generalization.

For Task 2, Fig. 19 (c) compares specificity scores, measuring the ability to correctly identify negative cases. While several teams maintain similar specificity across datasets, deviations suggest dataset-driven variability. Fig. 19 (d) presents the Quadratic Weighted Kappa, assessing ordinal classification agreement. The observed differences indicate that models trained on Brest may not generalize optimally to Algeria, reinforcing the impact of dataset characteristics.

Fig. 19 (e) quantifies ranking differences between Brest and Algeria. Positive values indicate better performance in Brest, while negative values reflect superior results in Algeria. This highlights teams with dataset-dependent strengths. Fig. 19 (f) illustrates ranking transitions across tasks, revealing trends in consistency or fluctuation. Stable rankings suggest robust performance across tasks, whereas pronounced shifts indicate varying task-specific strengths.

Overall, these results emphasize the influence of dataset properties on model performance and ranking consistency. The observed discrepancies suggest that while some teams achieve stable rankings, others experience significant variability, underlining the challenges of generalizing performance across different datasets.

The overall analysis reveals variations in ranking consistency across tasks, with some teams showing stable performance while others exhibit fluctuations. These results emphasize the importance of dataset characteristics and ranking methodologies in determining final placements.

In particular, teams such as MIPLAB, MIC Group 6 and FERLIV, which performed well on the Brest dataset (Table 7), maintained a relatively high ranking on the dataset from Tlemcens (Table 10). Conversely, teams like DF41 and STEP experienced a notable drop in ranking when applied to the dataset from Tlemcens, indicat-

ing a potential lack of robustness in handling distribution shifts.

These findings underscore the importance of developing models that generalize effectively across diverse datasets, highlighting the need for further research into domain adaptation and transfer learning techniques within medical imaging applications.

### 6.6. Model Parameters and Competition Performance

Our analysis of model parameters versus competition performance reveals several important insights into effective medical image analysis strategies. Panels A and B in Figure 20 demonstrate that the relationship between model size and ranking follows a non-linear pattern, challenging the assumption that larger models inherently perform better. In Task 1, smaller but well-designed architectures like "yyama" (31M parameters) and "scyyd4" (150M parameters) secured 2nd and 4th places respectively, outperforming several models with substantially larger parameter counts. This pattern suggests that architectural design choices and training approach can be more significant than raw parameter count.

Panel C introduces an efficiency metric (ranking  $\times$  100  $\div$  parameters) that identifies teams achieving strong performance with minimal computational resources. Interestingly, while MIPLAB employed a relatively large model (320M parameters), their first-place finish in both tasks resulted in competitive efficiency scores despite the higher parameter count. This demonstrates that parameter efficiency alone doesn't guarantee optimal performance in complex medical imaging tasks—model architecture and training methodology remain crucial factors.

The efficiency analysis further reveals that foundation models, particularly RetFound (marked with stars in Panel C), provided teams with significant advantages. Four of the top six teams incorporated RetFound in at least one task (Panel D), suggesting that models pre-trained on relevant medical imaging datasets offer substantial benefits over training from scratch, even when controlling for model size.

Framework selection showed strong convergence, with PyTorch dominating as the preferred development environment across all competing teams. However, the non-linear trend lines in Panels A, B, and D indicate diminishing returns from simply scaling model size, particularly evident in the U-shaped curve of Panel B where mid-sized models struggled relative to both smaller and larger architectures.

These findings highlight that successful medical image analysis depends more on thoughtful model selec-

tion, effective pre-training, and task-specific optimization than on pursuing increasingly larger architectures. The results emphasize the value of foundation models like RetFound that encode domain-specific knowledge while maintaining reasonable computational requirements.

### 6.7. Evaluation of Ranking stability

While the final competition ranking was determined solely based on performance on the Brest dataset, it is essential to evaluate the stability and significance of these rankings across datasets. This section presents two complementary analyses: (1) a ranking bootstrap analysis to assess variability under resampling, and (2) statistical significance testing to determine whether observed performance differences between teams are meaningful.

#### 6.7.1. Ranking bootstrapping

To estimate the stability of the rankings, we employed a bootstrap resampling procedure, following the methodology proposed by Wiesenfarth et al. Wiesenfarth et al. (2021). This involves resampling predictions with replacement and recalculating performance metrics over multiple iterations to generate a distribution of rankings for each team.

This analysis allows us to quantify the confidence in each team's rank and identify potential overlaps in ranking distributions. For example, teams that appear close in the final leaderboard but have overlapping ranking distributions may not be statistically distinguishable in performance.

Bootstrap-based ranking intervals (e.g., 95% confidence bands) are reported to visualize uncertainty and support robust ranking interpretation beyond point estimates.

As illustrated in Figure 21, the bootstrapped performance distributions (left) show the relative scores achieved by each team per task and overall. The corresponding rank stability plots (right) demonstrate the consistency of team rankings under sampling variability, revealing greater rank volatility in Tlemcen compared to Brest.

#### 6.7.2. McNemar Test for Model Comparisons

To further assess pairwise differences between models, particularly in binary classification performance, we conducted the McNemar test on the prediction outputs. This non-parametric test evaluates whether two classifiers have significantly different proportions of errors on paired data.

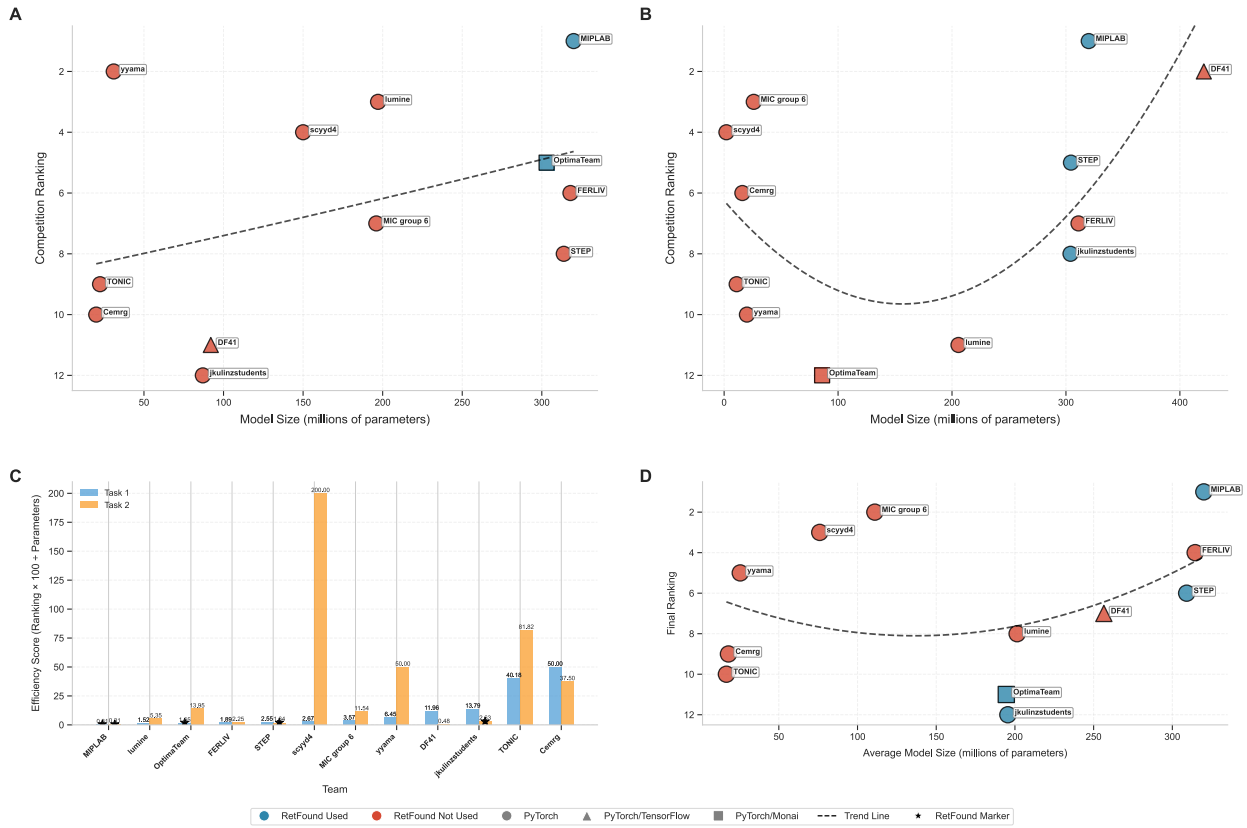


Figure 20: Relationship between model complexity, framework choice, and performance across competition tasks. Panels A and B illustrate the relationship between model size (parameters in millions) and ranking for Task 1 (structural classification) and Task 2 (disease progression prediction), respectively. Panel C quantifies efficiency (ranking  $\times$  100  $\div$  parameters) across both tasks, with star markers indicating RetFound usage. Panel D plots average model size against final competition ranking. Blue markers represent teams using RetFound in at least one task, while red markers indicate teams that did not. Marker shapes denote frameworks (circle: PyTorch, triangle: PyTorch/TensorFlow, square: PyTorch/Monai). Dashed lines represent polynomial trend lines.

For each team pair, we computed a contingency table of their prediction disagreements and used the McNemar test to assess significance.  $p$ -values were corrected for multiple comparisons using the Benjamini-Hochberg procedure to control the false discovery rate.

This statistical evaluation reveals whether observed performance differences between teams are statistically significant or fall within the margin of random variation—providing a more nuanced perspective on leaderboard outcomes.

Figure 22 shows pairwise statistical comparisons of team predictions using McNemar’s test. Denser clusters of significant differences appear in Task 2 for both Brest and Tlemcen, suggesting higher variability and divergence in team strategies or performance for this task.

## 7. Discussion

The MARIO challenge attracted a diverse array of methodologies leveraging state-of-the-art deep learning techniques for medical image analysis. It served as a valuable benchmark for assessing the efficacy of various computational strategies, particularly in multi-modal learning and pretraining methodologies. This section presents a comprehensive analysis of key trends, highlighting both advancements and limitations observed among participants, while also discussing the broader clinical significance of the challenge outcomes. Additionally, we propose future directions to address current shortcomings and further refine research in this domain. Notably, 100% of the participating teams implemented their solutions using the PyTorch framework Paszke et al. (2019). This strong adoption of PyTorch mirrors observations from other data challenges Andreańczyk et al. (2023); Nwoye et al. (2023); Dorent et al.

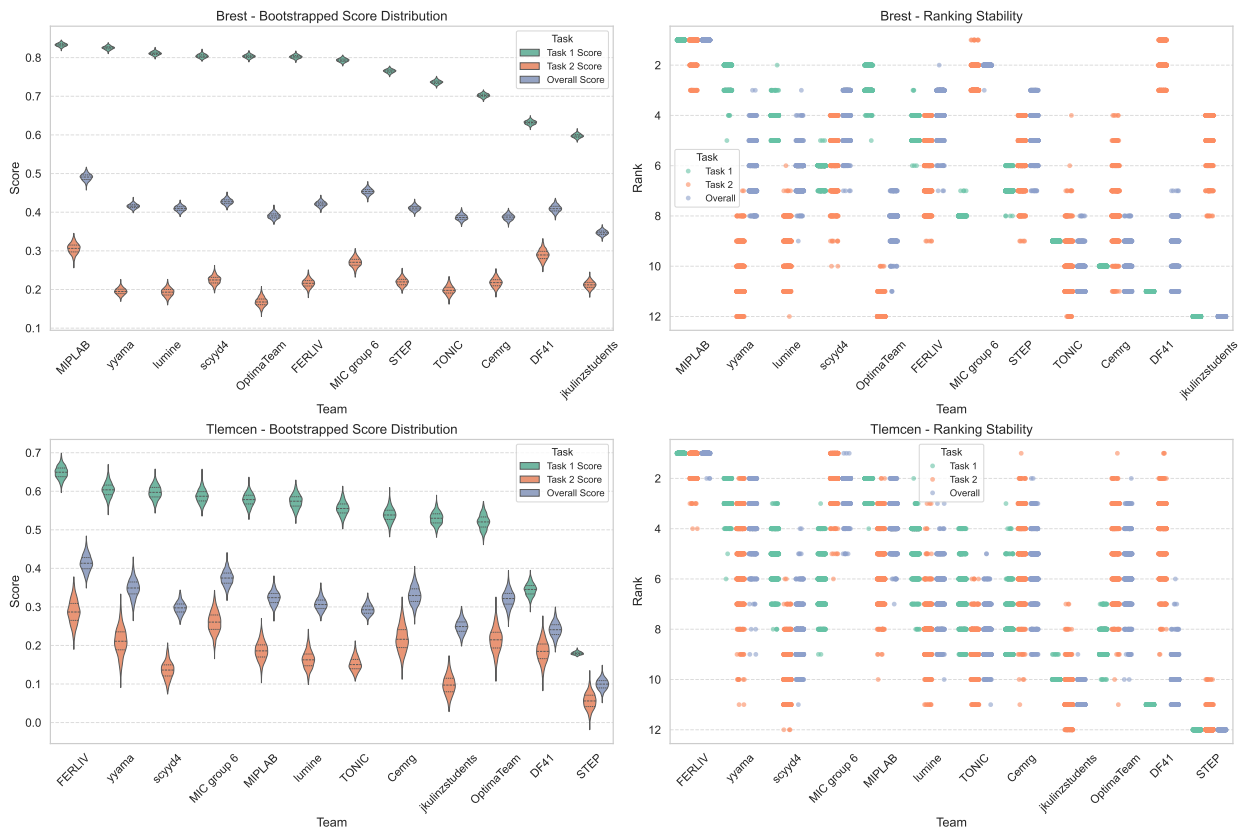


Figure 21: Comparison of bootstrapped performance across teams in **Brest** (top row) and **Tlemcen** (bottom row). Left column: Score distributions from bootstrapped metrics (Task 1, Task 2, and Overall), visualized using violin plots. Right column: Rank stability of each team computed from 500 bootstrap iterations, where each point represents the ranking of a team for a single bootstrap sample. Lower ranks indicate better performance. This visualization highlights both performance magnitude and ranking consistency under resampling.

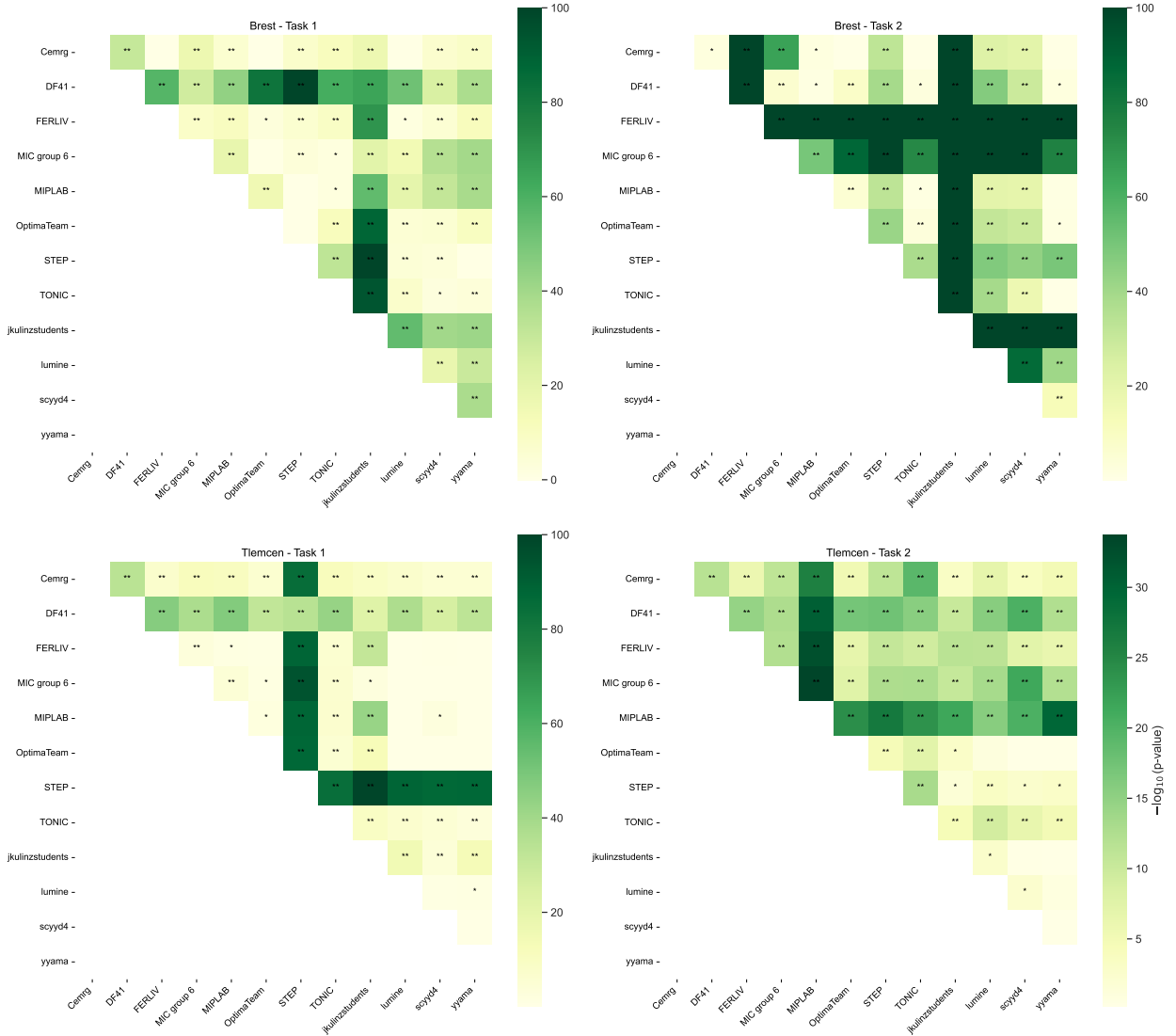


Figure 22: McNemar test results for pairwise comparisons of team predictions on both tasks in **Brest** (top row) and **Tlemcen** (bottom row). Each cell represents  $-\log_{10}(p)$  for a McNemar test between two models. Only statistically significant values (i.e.,  $p < 0.01$ ) are shown in the upper triangle of the matrix. Asterisks denote significance levels (\* for  $p < 0.001$ , \*\* for  $p < 0.0001$ ). These heatmaps highlight which teams produce significantly different predictions, with denser significance patterns observed in Task 2 across both cities.

(2023), where it consistently emerges as the preferred framework for developing deep learning-based research methodologies aoun et al. (2022).

### 7.1. Popular Baseline Approaches

Several teams adopted commonly used baseline models that served as foundational approaches in the challenge:

**One-head model:** A straightforward classification model with a single output head. **Siamese network:** Designed to capture differences between consecutive OCT scans by leveraging a dual-branch architecture.

These baseline models provided a strong foundation upon which teams developed more sophisticated methods.

### 7.2. Custom Elements Proposed

The following section outlines key modifications and enhancements implemented by the finalists to personalize their solutions and augment the common baseline.

#### 7.2.1. Loss Functions

**OPTIMA Team:** Recognizing the ordinal nature of the change labels, the team incorporated a discrete Wasserstein-2 loss to exploit the ordinality effectively. To improve robustness, they employed a majority voting mechanism across three models to produce a single, more reliable prediction.

#### 7.2.2. Custom Neural Network Blocks

**STEP Team:** Introduced a bidirectional cross-attention module designed to capture dependencies between sequential B-scan pairs. CLS tokens extracted from the B-scans were processed to compute temporal relationships, with cross-attention enhancing the model’s sensitivity to subtle disease progression changes. A linear layer generated individual predictions for each B-scan, with predictions aggregated using batched inference for OCT volumes. A Multiple Instance Learning (MIL)-based architecture was further developed for identifying the most significant slices within an OCT volume for predicting disease progression.

**FERLIV Team:** Proposed a modular, fully transformer-based approach using three transformer encoder architectures: Feature Encoder, Change Encoder, and Diagnosis Encoder. The Feature Encoder utilized a Vision Transformer to extract local feature vectors from OCT scans, while the Change Encoder employed a dual Multi-Change Captioning Transformer with a co-attention mechanism to detect visual changes. Finally,

the Diagnosis Encoder quantified changes in disease progression using self-attention mechanisms, followed by a classification head.

#### 7.2.3. Data Entry Enhancements

Some teams explored novel data representations, such as concatenating consecutive OCT or infrared images to better leverage temporal context and improve predictive accuracy.

### 7.3. Multi-Modal Learning

A key trend observed in the challenge was the adoption of multi-modal learning approaches. Multi-modal fusion allows models to integrate complementary information from diverse data sources, enhancing predictive performance and robustness. Teams such as **MIPLAB** effectively integrated OCT scans, localizer images, and clinical variables to construct a comprehensive representation of disease pathology. Similarly, **MIC Group 6** and **Jkstudents** demonstrated the effectiveness of multi-modal embeddings, leveraging pretext task features from Task 1 to refine predictions in Task 2.

Despite the success of multi-modal approaches, only a limited number of teams implemented them, indicating significant untapped potential. Future research should explore integrating additional modalities such as fluorescein angiography, patient demographics, and genetic markers to improve diagnostic accuracy. Additionally, the application of transformer-based architectures and self-attention mechanisms in multi-modal fusion remains an area of promising exploration.

Standardized frameworks for multi-modal fusion are also necessary to ensure effective harmonization of different data types. Furthermore, interpretability remains a critical challenge, as clinical practitioners require transparent decision-making processes to validate model predictions.

### 7.4. Pretraining Strategies

Pretraining on large-scale datasets was a crucial determinant of success in the challenge. Participants employed various pretraining paradigms, ranging from conventional supervised learning on natural image datasets to domain-specific self-supervised learning approaches. Teams such as **Lumine** and **TONIC** leveraged pretrained architectures like ConvNeXt and ResNet, initialized with ImageNet weights. Conversely, The **FERLIV** team performed additional fine-tuning of the RETFound weights in the pretext task on the public retinal layer segmentation dataset. And **MIPLAB** utilized domain-specific pretraining via RETFound, a

model explicitly designed for retinal imaging, capitalizing on knowledge from similar datasets.

The superior performance of domain-specific pretraining over generic pretraining underscores the importance of large-scale, domain-relevant datasets for enhancing model generalizability. Additionally, some teams, such as **OPTIMA**, explored self-supervised learning approaches, including masked autoencoders, to learn meaningful latent representations from unlabeled data. A systematic evaluation of pretraining strategies—particularly the comparative benefits of supervised, self-supervised, and hybrid approaches—remains an open area for further research.

Future efforts should focus on developing benchmark datasets for pretraining in ophthalmology, incorporating a diverse range of pathologies and imaging conditions. Contrastive learning techniques, which have demonstrated success in other medical imaging applications, could also be explored to improve feature representations in retinal image analysis.

### 7.5. Generative Approaches

Several teams leveraged generative methods to enhance disease progression prediction:

**MIC Group 6:** Developed a hybrid framework to predict AMD progression using a single OCT scan, building upon pretraining insights from Task 1. The Siamese Network with an ImageNet encoder emerged as the top-performing model, demonstrating superior feature extraction capabilities.

**Jkstudents:** Implemented a two-step deep learning approach comparable to the BYOL framework, utilizing the next exam in time as augmentation to enhance predictive accuracy.

**DF41:** Introduced the Patch Progression Masked Autoencoder (PPMAE) to predict a future OCT image based on the current scan. The model masked 75% of the current OCT image and predicted the corresponding patches from the follow-up image, allowing it to capture temporal changes and disease progression effectively. This method improved the model’s ability to anticipate future disease states based on historical imaging data.

### 7.6. Feature-Based Strategies

Feature extraction methods played a significant role in multi-modal learning:

**MIPLAB:** Utilized RETFound to extract features from OCT and infrared images, which were subsequently used as inputs for a multi-modal machine learning model. This approach demonstrated the effectiveness of feature-based strategies in improving diagnostic accuracy.

### 7.7. Limitations and Future Directions

The MARIO challenge provided a valuable platform for evaluating cutting-edge deep learning methodologies in medical image analysis. Key trends, such as multi-modal learning, domain-specific pretraining, and generative approaches, emerged as significant drivers of success. However, several challenges remain, including limited adoption of multi-modal strategies, the need for standardized pretraining datasets, and the necessity of improved interpretability for clinical applications.

While the MARIO challenge facilitated significant advancements in medical image analysis, several limitations were observed, which provide critical insights for future iterations of the competition and broader research efforts.

- 1. Data Augmentation and Diversity:** Most teams implemented conventional augmentation techniques such as cropping, flipping, and color jittering. However, the use of synthetic data generation techniques, such as generative adversarial networks (GANs) and diffusion models was relatively underexplored. These approaches could play a crucial role in addressing class imbalances and enhancing model robustness by augmenting under-represented pathological cases.
- 2. Over-reliance on Public Datasets:** A considerable number of teams pretrained their models on ImageNet and other general-purpose datasets, which may not align well with the specialized nature of the challenge. While domain-specific models such as RETFound demonstrated superior performance, the lack of large-scale, publicly available ophthalmic datasets remains a bottleneck. Future work should focus on curating diverse, high-quality datasets for improved model training and evaluation.
- 3. Explainability and Interpretability:** Despite high predictive performance, few models prioritized explainability, which is essential for clinical adoption. Methods such as saliency maps, class activation mappings, and attention mechanisms should be further explored to provide clear justifications for model predictions, thereby enhancing trust among clinicians.
- 4. Generative Techniques:** Teams such as **Jkstudents** and **MIC Group 6** demonstrated the potential of synthetic scans in Task 2, but broader adoption of generative models could enhance dataset diversity and improve generalizability. Future work should consider exploring diffusion models and

variational autoencoders (VAEs) for more effective synthetic data generation.

Beyond addressing these limitations, future editions of the challenge could introduce additional tasks that reflect more clinically relevant scenarios. Some proposed directions include:

- **Integration of Anti-VEGF Treatment Context:** A dedicated task could be introduced to incorporate patient treatment history, specifically anti-VEGF therapy, as an additional predictive variable. This would provide a more comprehensive understanding of disease progression and treatment response, ultimately improving clinical decision support.
- **Volume-Based Pathology Prediction:** Instead of limiting pathology predictions to individual slices (B-scan level), future challenges could introduce volumetric predictions (C-scan level). This shift would align more closely with clinical assessment practices, where volumetric changes provide critical insights into disease progression.
- **Federated Learning for Privacy-Preserving Model Training:** Given the sensitivity of medical data, future iterations of the challenge could explore federated learning paradigms, enabling models to be trained across multiple institutions without sharing raw patient data. This would facilitate the development of more generalized and privacy-conscious AI models.
- **Incorporation of Temporal Analysis:** Longitudinal analysis of disease progression using time-series OCT scans could be introduced as a novel task. Predicting future disease states based on past imaging data would be highly valuable for clinical prognostics and treatment planning.

By addressing these aspects, future editions of the MARIO challenge can further drive innovation in medical image analysis, ultimately contributing to the development of more accurate, interpretable, and clinically relevant AI solutions.

For Task 1, participants provided technical solutions with excellent performance, demonstrating their potential for clinical use. However, Task 2 remains a significant challenge. While participants were highly innovative and explored various approaches, no team achieved satisfactory results. We have outlined above the different directions that could help advance this area in future editions.

## Data Availability

The dataset has been made publicly available via Zenodo<sup>5</sup>. To ensure consistency and reproducibility, we adhered to the original data split and folder structure that were provided during the challenge phase. Currently, only the dataset from Brest has been released publicly. The Tlemcen dataset, due to privacy and regulatory considerations, remains private and is not available for distribution at this time.

## Declaration of generative AI in scientific writing

During the preparation of this work the author(s) used LLM(s) in order to improve readability and language. After using this tool/service, the author(s) reviewed and edited the content as needed and take(s) full responsibility for the content of the publication.

## Acknowledgements

This work is conducted within the framework of the **Eviored** project, a research initiative funded by the French National Research Agency (*Agence Nationale de la Recherche*, ANR) as part of the *RHU* program. It has received financial support from the French government under the “*Investissements d’Avenir*” program, with the reference **ANR-18-RHUS-0008**.

We extend our gratitude to the **CHU of Brest** for their significant contributions to patient care and for their efforts in constructing the dataset. We particularly acknowledge the valuable time and expertise of the medical professionals who meticulously annotated the data, ensuring its quality and reliability.

Furthermore, we sincerely thank the **Lazouni Clinic** for granting access to the Algerian dataset and for their essential role in patient care. We also acknowledge the dedicated efforts of the medical team in providing expert annotations, which were instrumental in the success of this study.

## References

- N. M. Schultz, S. Bhardwaj, C. Barclay, L. Gaspar, J. Schwartz, Global burden of dry age-related macular degeneration: A targeted literature review, *Clinical Therapeutics* 43 (2021) 1792–1818. URL: <https://www.sciencedirect.com/science/article/pii/S0149291821003106>.

<sup>5</sup><https://zenodo.org/records/15270469>

- doi:<https://doi.org/10.1016/j.clinthera.2021.08.011>.
- W. L. Wong, X. Su, X. Li, C. M. G. Cheung, R. Klein, C.-Y. Cheng, T. Y. Wong, Global prevalence of age-related macular degeneration and disease burden projection for 2020 and 2040: a systematic review and meta-analysis, *The Lancet Global Health* 2 (2014) e106–e116.
- M. Fleckenstein, P. Mitchell, K. B. Freund, S. Sadda, F. G. Holz, C. Brittain, E. C. Henry, D. Ferrara, Age-related macular degeneration, *Nature Reviews Disease Primers* 4 (2018) 1–19.
- P. J. Rosenfeld, D. M. Brown, J. S. Heier, D. S. Boyer, P. K. Kaiser, C. Y. Chung, R. Y. Kim, Ranibizumab for neovascular age-related macular degeneration, *New England Journal of Medicine* 355 (2006) 1419–1431. URL: <https://doi.org/10.1056/nejmoa054481>. doi:10.1056/nejmoa054481.
- D. M. Brown, P. K. Kaiser, M. Michels, G. Soubrane, J. S. Heier, R. Y. Kim, J. P. Sy, S. Schneider, Ranibizumab versus verteporfin for neovascular age-related macular degeneration, *New England Journal of Medicine* 355 (2006) 1432–1444.
- J. Yim, R. Chopra, T. Spitz, J. Winkens, A. Obika, C. Kelly, H. Askham, M. Lukic, J. Huemer, K. Fasler, et al., Predicting conversion to wet age-related macular degeneration using deep learning, *Nature Medicine* 26 (2020) 892–899.
- F. Grassmann, J. Mengelkamp, C. Brandl, S. Harsch, M. E. Zimmermann, B. Linkohr, A. Peters, I. M. Heid, C. Palm, B. H. Weber, A deep learning algorithm for prediction of age-related eye disease study severity scale for age-related macular degeneration from color fundus photography, *Ophthalmology* 125 (2018) 1410–1420.
- U. Schmidt-Erfurth, G. S. Reiter, S. Riedl, P. Seeböck, W.-D. Vogl, B. A. Blodi, A. Domalpally, A. Fawzi, Y. Jia, D. Sarraf, H. Bogunović, Ai-based monitoring of retinal fluid in disease activity and under therapy, *Progress in Retinal and Eye Research* 86 (2022) 100972. URL: <http://dx.doi.org/10.1016/j.preteyeres.2021.100972>. doi:10.1016/j.preteyeres.2021.100972.
- P. Lanzetta, A. Loewenstein, V. A. S. Committee, et al., Fundamental principles of an anti-vegf treatment regimen: optimal application of intravitreal anti-vascular endothelial growth factor therapy of macular diseases, *Graefe's Archive for Clinical and Experimental Ophthalmology* 259 (2021) 2097–2109.
- G. A. Lalwani, P. J. Rosenfeld, A. E. Fung, S. R. Dubovy, S. Michels, W. Feuer, J. L. Davis, H. W. Flynn Jr, M. Esquiabro, A variable-dosing regimen with intravitreal ranibizumab for neovascular age-related macular degeneration: year 2 of the pronto study, *American journal of ophthalmology* 148 (2009) 43–58.
- K. B. Freund, J.-F. Korobelnik, R. Devenyi, C. Framme, J. Galic, E. Herbert, H. Hoerauf, P. Lanzetta, S. Michels, P. Mitchell, J. Monés, C. Regillo, R. Tadayoni, J. Talks, S. Wolf, TREAT-AND-EXTEND REGIMENS WITH ANTI-VEGF AGENTS IN RETINAL DISEASES, *Retina* 35 (2015) 1489–1506. URL: <https://doi.org/10.1097/iae.0000000000000627>. doi:10.1097/iae.0000000000000627.
- U. Schmidt-Erfurth, S. M. Waldstein, S. Klmscha, A. Sadeghipour, X. Hu, B. S. Gerendas, A. Osborne, H. Bogunović, Machine learning to analyze the prognostic value of current imaging biomarkers in neovascular age-related macular degeneration, *Ophthalmology Retina* 2 (2018) 24–30.
- M. S. Blumenkranz, J. A. Haller, B. D. Kuppermann, G. A. Williams, M. Ip, M. Davis, D. V. Weinberg, C. Chou, S. M. Whitcup, Correlation of visual acuity and macular thickness measured by optical coherence tomography in patients with persistent macular edema, *Retina* 30 (2010) 1090–1094. URL: <http://dx.doi.org/10.1097/IAE.0b013e3181dcfaf3>. doi:10.1097/iae.0b013e3181dcfaf3.
- S. Sharma, C. A. Toth, E. Daniel, J. E. Grunwald, M. G. Maguire, G.-s. Ying, J. Huang, D. F. Martin, G. J. Jaffe, C. of Age-related Macular Degeneration Treatments Trials Research Group, et al., Macular morphology and visual acuity in the second year of the comparison of age-related macular degeneration treatments trials, *Ophthalmology* 123 (2016) 865–875.
- R. H. Guymer, C. M. Markey, I. L. McAllister, M. C. Gillies, A. P. Hunyor, J. J. Arnold, F. Investigators, et al., Tolerating subretinal fluid in neovascular age-related macular degeneration treated with ranibizumab using a treat-and-extend regimen: Fluid

- study 24-month results, *Ophthalmology* 126 (2019) 723–734.
- A. Lang, A. Carass, O. Al-Louzi, P. Bhargava, S. D. Solomon, P. A. Calabresi, J. L. Prince, Combined registration and motion correction of longitudinal retinal oct data, in: M. A. Styner, E. D. Angelini (Eds.), *Medical Imaging 2016: Image Processing*, volume 9784, SPIE, 2016, p. 97840X. URL: <http://dx.doi.org/10.1117/12.2217157>. doi:10.1117/12.2217157.
- M. Golabbakhsh, H. Rabbani, A full-reference three-component quality assessment metric for medical images, *2013 IEEE International Conference on Acoustics, Speech and Signal Processing (2013)* 1262–1266.
- C. Lea, M. D. Flynn, R. Vidal, A. Reiter, G. D. Hager, Temporal convolutional networks for action segmentation and detection, *Proceedings of the IEEE conference on computer vision and pattern recognition (2017)* 156–165.
- R. T. Chen, Y. Rubanova, J. Bettencourt, D. K. Duvenaud, Neural ordinary differential equations, *Advances in neural information processing systems* 31 (2018).
- A. Vaswani, N. Shazeer, N. Parmar, J. Uszkoreit, L. Jones, A. N. Gomez, Ł. Kaiser, I. Polosukhin, Attention is all you need, *Advances in neural information processing systems* 30 (2017).
- H. Liu, L. Li, I. M. Wormstone, C. Qiao, C. Zhang, P. Liu, S. Li, H. Wang, D. Mou, R. Pang, D. Yang, L. M. Zangwill, S. Moghimi, H. Hou, C. Bowd, L. Jiang, Y. Chen, M. Hu, Y. Xu, H. Kang, X. Ji, R. Chang, C. Tham, C. Cheung, D. S. W. Ting, T. Y. Wong, Z. Wang, R. N. Weinreb, M. Xu, N. Wang, Development and validation of a deep learning system to detect glaucomatous optic neuropathy using fundus photographs, *JAMA Ophthalmology* 137 (2019) 1353–1360. URL: <https://doi.org/10.1001/jamaophthol.2019.3501>. doi:10.1001/jamaophthol.2019.3501. arXiv:<https://jamanetwork.com/journals/jamaophthol/article-abstract/2749507>
- E. Crincoli, R. Sacconi, L. Querques, G. Querques, Artificial intelligence in age-related macular degeneration: state of the art and recent updates, *BMC Ophthalmology* 24 (2024). URL: <http://dx.doi.org/10.1186/s12886-024-03381-1>. doi:10.1186/s12886-024-03381-1.
- K. Romond, M. Alam, S. Kravets, L. d. Sisternes, T. Leng, J. I. Lim, D. Rubin, J. A. Hallak, Imaging and artificial intelligence for progression of age-related macular degeneration, *Experimental Biology and Medicine* 246 (2021) 2159–2169. URL: <http://dx.doi.org/10.1177/15353702211031547>. doi:10.1177/15353702211031547.
- G. A. Muntean, A. Marginean, A. Groza, I. Damian, S. A. Roman, M. C. Hapca, M. V. Muntean, S. D. Nicoară, The predictive capabilities of artificial intelligence-based oct analysis for age-related macular degeneration progression—a systematic review, *Diagnostics* 13 (2023) 2464. URL: <http://dx.doi.org/10.3390/diagnostics13142464>. doi:10.3390/diagnostics13142464.
- U. Schmidt-Erfurth, S. Klmscha, S. M. Waldstein, H. Bogunović, A view of the current and future role of optical coherence tomography in the management of age-related macular degeneration, *Eye* 31 (2016) 26–44. URL: <http://dx.doi.org/10.1038/eye.2016.227>. doi:10.1038/eye.2016.227.
- B. Hassan, S. Qin, R. Ahmed, T. Hassan, A. H. Taguri, S. Hashmi, N. Werghe, Deep learning based joint segmentation and characterization of multi-class retinal fluid lesions on OCT scans for clinical use in anti-VEGF therapy, *Computers in Biology and Medicine* 136 (2021) 104727. URL: <https://www.sciencedirect.com/science/article/pii/S0010482521005217>. doi:<https://doi.org/10.1016/j.compbimed.2021.104727>.
- T. Schlegl, S. M. Waldstein, H. Bogunovic, F. Endstraß, A. Sadeghipour, A.-M. Philip, D. Podkowinski, B. S. Gerendas, G. Langs, U. Schmidt-Erfurth, Fully automated detection and quantification of macular fluid in oct using deep learning, *Ophthalmology* 125 (2018) 549–558.
- F. G. Venhuizen, B. van Ginneken, B. Liefers, M. J. van Grinsven, S. Fauser, C. Hoyng, T. Theelen, C. I. Sánchez, Deep learning approach for the detection and quantification of epiretinal membranes, *Ophthalmology* 125 (2018) 1545–1569. URL: <https://doi.org/10.1016/j.ophtha.2018.03.011>
- K. Xu, S. Huang, Z. Yang, Y. Zhang, Y. Fang, G. Zheng, B. Lin, M. Zhou, J. Sun, Automatic detection and differential diagnosis of age-related macular degeneration from color fundus photographs

- using deep learning with hierarchical vision transformer, *Computers in Biology and Medicine* 167 (2023) 107616. URL: <http://dx.doi.org/10.1016/j.combiomed.2023.107616>. doi:10.1016/j.combiomed.2023.107616.
- M. Melinščak, Attention-based u-net: Joint segmentation of layers and fluids from retinal oct images, in: 2023 46th MIPRO ICT and Electronics Convention (MIPRO), IEEE, 2023, p. 391–396. URL: <http://dx.doi.org/10.23919/MIPRO57284.2023.10159914>. doi:10.23919/mipro57284.2023.10159914.
- A. G. Roy, S. Conjeti, S. P. K. Karri, D. Sheet, A. Kattouzian, C. Wachinger, N. Navab, Relaynet: retinal layer and fluid segmentation of macular optical coherence tomography using fully convolutional networks, *Biomedical optics express* 8 (2017) 3627–3642.
- C. Simader, M. Ritter, M. Bolz, G. G. Deák, U. Mayr-Sponer, I. Golbazi, M. Kundi, U. M. Schmidt-Erfurth, Morphologic parameters relevant for visual outcome during anti-angiogenic therapy of neovascular age-related macular degeneration, *Ophthalmology* 121 (2014) 1237–1245.
- A. Rivail, U. Schmidt-Erfurth, W.-D. Vogl, S. M. Waldstein, S. Riedl, C. Grechenig, Z. Wu, H. Bogunovic, Modeling disease progression in retinal octs with longitudinal self-supervised learning, in: *Predictive Intelligence in Medicine: Second International Workshop, PRIME 2019, Held in Conjunction with MICCAI 2019, Shenzhen, China, October 13, 2019, Proceedings 2*, Springer, 2019, pp. 44–52.
- J. Jung, J. Han, J. M. Han, J. Ko, J. Yoon, J. S. Hwang, J. I. Park, G. Hwang, J. H. Jung, D. D.-J. Hwang, Prediction of neovascular age-related macular degeneration recurrence using optical coherence tomography images with a deep neural network, *Scientific Reports* 14 (2024). URL: <http://dx.doi.org/10.1038/s41598-024-56309-6>. doi:10.1038/s41598-024-56309-6.
- E. M. Lad, K. Sleiman, D. L. Banks, S. Hariharan, T. Clemons, R. Herrmann, D. Dauletbekov, A. Giani, V. Chong, E. Y. Chew, C. A. Toth, C. A. Toth, W. Wong, T. Huang, G. B. Hubbard, S. Srivastava, M. McCall, K. Winter, N. Sarin, K. Hall, P. McCollum, L. Curtis, S. Schuman, S. J. Chiu, S. Farsi, V. Tai, T. Clemons, E. Chew, Machine learning oct predictors of progression from intermediate age-related macular degeneration to geographic atrophy and vision loss, *Ophthalmology Science* 2 (2022) 100160. URL: <http://dx.doi.org/10.1016/j.xops.2022.100160>. doi:10.1016/j.xops.2022.100160.
- B. Yellapragada, S. Hornauer, K. Snyder, S. Yu, G. Yiu, Self-supervised feature learning and phenotyping for assessing age-related macular degeneration using retinal fundus images, *Ophthalmology Retina* 6 (2022) 116–129. URL: <http://dx.doi.org/10.1016/j.oret.2021.06.010>. doi:10.1016/j.oret.2021.06.010.
- A. Chakravarty, T. Emre, O. Leingang, S. Riedl, J. Mai, H. P. N. Scholl, S. Sivaprasad, D. Rueckert, A. Lotery, U. Schmidt-Erfurth, H. Bogunović, Morph-ssl: Self-supervision with longitudinal morphing for forecasting amd progression from oct volumes, *IEEE Transactions on Medical Imaging* 43 (2024) 3224–3239. URL: <http://dx.doi.org/10.1109/TMI.2024.3390940>. doi:10.1109/tmi.2024.3390940.
- J. Kugelmann, D. Alonso-Caneiro, S. A. Read, M. J. Collins, A review of generative adversarial network applications in optical coherence tomography image analysis, *Journal of Optometry* 15 (2022) S1–S11.
- S. Matta, M. Lamard, P. Zhang, A. Le Guilcher, L. Borderie, B. Cochener, G. Quéllec, A systematic review of generalization research in medical image classification, *Computers in Biology and Medicine* 183 (2024) 109256. URL: <https://www.sciencedirect.com/science/article/pii/S0010482524013416>. doi:<https://doi.org/10.1016/j.combiomed.2024.109256>.
- H. Guan, M. Liu, Domain adaptation for medical image analysis: a survey, *IEEE Transactions on Biomedical Engineering* 69 (2021) 1173–1185.
- X. Liu, C. Yoo, F. Xing, H. Oh, G. El Fakhri, J.-W. Kang, J. Woo, et al., Deep unsupervised domain adaptation: A review of recent advances and perspectives, *APSIPA Transactions on Signal and Information Processing* 11 (2022).
- A. Gomariz, H. Lu, Y. Y. Li, T. Albrecht, A. Maunz, F. Benmansour, A. M. Valcarcel, J. Luu, D. Ferrara, O. Goksel, Unsupervised Domain Adaptation with Contrastive Learning for

- OCT Segmentation, Springer Nature Switzerland, 2022, p. 351–361. URL: [http://dx.doi.org/10.1007/978-3-031-16452-1\\_34](http://dx.doi.org/10.1007/978-3-031-16452-1_34). doi:10.1007/978-3-031-16452-1\_34.
- D. Ueda, T. Kakinuma, S. Fujita, K. Kamagata, Y. Fushimi, R. Ito, Y. Matsui, T. Nozaki, T. Nakaura, N. Fujima, et al., Fairness of artificial intelligence in healthcare: review and recommendations, *Japanese Journal of Radiology* 42 (2024) 3–15.
- J. I. Lim, A. V. Rachitskaya, J. A. Hallak, S. Gholami, M. N. Alam, Artificial intelligence for retinal diseases, *Asia-Pacific Journal of Ophthalmology* 13 (2024) 100096. URL: <https://www.sciencedirect.com/science/article/pii/S2162098924000975>. doi:<https://doi.org/10.1016/j.apjo.2024.100096>.
- H. Bogunovic, F. Venhuizen, S. Klimscha, S. Apostolopoulos, A. Bab-Hadiashar, U. Bagci, M. F. Beg, L. Bekalo, Q. Chen, C. Ciller, K. Gopinath, A. K. Gostar, K. Jeon, Z. Ji, S. H. Kang, D. D. Koozekanani, D. Lu, D. Morley, K. K. Parhi, H. S. Park, A. Rashno, M. Sarunic, S. Shaikh, J. Sivaswamy, R. Tennakoon, S. Yadav, S. De Zanet, S. M. Waldstein, B. S. Gerendas, C. Klaver, C. I. Sanchez, U. Schmidt-Erfurth, Retouch: The retinal oct fluid detection and segmentation benchmark and challenge, *IEEE Transactions on Medical Imaging* 38 (2019) 1858–1874. URL: <http://dx.doi.org/10.1109/TMI.2019.2901398>. doi:10.1109/tmi.2019.2901398.
- M. Díaz, J. Novo, P. Cutrín, F. Gómez-Ulla, M. G. Penedo, M. Ortega, Automatic segmentation of the foveal avascular zone in ophthalmological oct-a images, *PLOS ONE* 14 (2019) e0212364. URL: <http://dx.doi.org/10.1371/journal.pone.0212364>. doi:10.1371/journal.pone.0212364.
- L. Maier-Hein, M. Eisenmann, A. Reinke, S. Onogur, M. Stankovic, P. Scholz, T. Arbel, H. Bogunovic, A. P. Bradley, A. Carass, C. Feldmann, A. F. Frangi, P. M. Full, B. van Ginneken, A. Hanbury, K. Honauer, M. Kozubek, B. A. Landman, K. März, O. Maier, K. Maier-Hein, B. H. Menze, H. Müller, P. F. Neher, W. Niessen, N. Rajpoot, G. C. Sharp, K. Sirinukunwattana, S. Speidel, C. Stock, D. Stoyanov, A. A. Taha, F. van der Sommen, C.-W. Wang, M.-A. Weber, G. Zheng, P. Jannin, A. Kopp-Schneider, Why rankings of biomedical image analysis competitions should be interpreted with care, *Nature Communications* 9 (2018). URL: <https://doi.org/10.1038/s41467-018-07619-7>. doi:10.1038/s41467-018-07619-7.
- Z. Xu, S. Escalera, A. Pavão, M. Richard, W.-W. Tu, Q. Yao, H. Zhao, I. Guyon, Codabench: Flexible, easy-to-use, and reproducible meta-benchmark platform, *Patterns* 3 (2022) 100543. URL: <https://www.sciencedirect.com/science/article/pii/S2666389922001465>. doi:<https://doi.org/10.1016/j.patter.2022.100543>.
- A. R. Rudnicka, Z. Jarrar, R. Wormald, D. G. Cook, A. Fletcher, C. G. Owen, Age and gender variations in age-related macular degeneration prevalence in populations of european ancestry: A meta-analysis, *Ophthalmology* 119 (2012) 571–580. URL: <http://dx.doi.org/10.1016/j.optha.2011.09.027>. doi:10.1016/j.optha.2011.09.027.
- G. Quellec, J. Kowal, P. W. Hasler, H. P. N. Scholl, S. Zweifel, B. Konstantinos, J. E. R. Carvalho, T. Heeren, C. Egan, A. Tufail, P. M. Maloca, Feasibility of support vector machine learning in age-related macular degeneration using small sample yielding sparse optical coherence tomography data, *Acta Ophthalmologica* 97 (2019). URL: <https://doi.org/10.1111/aos.14055>. doi:10.1111/aos.14055.
- A. Kolesnikov, A. Dosovitskiy, D. Weissenborn, G. Heigold, J. Uszkoreit, L. Beyer, M. Minderer, M. Dehghani, N. Houlsby, S. Gelly, T. Unterthiner, X. Zhai, An image is worth 16x16 words: Transformers for image recognition at scale, 2021.
- Y. Qiu, S. Yamamoto, K. Nakashima, R. Suzuki, K. Iwata, H. Kataoka, Y. Satoh, Describing and localizing multiple changes with transformers, in: *Proceedings of the IEEE/CVF International Conference on Computer Vision*, 2021, pp. 1971–1980.
- J. Lu, D. Batra, D. Parikh, S. Lee, Vilbert: Pretraining task-agnostic visiolinguistic representations for vision-and-language tasks, *Advances in neural information processing systems* 32 (2019).
- Y. Zhou, M. A. Chia, S. K. Wagner, M. S. Ayhan, D. J. Williamson, R. R. Struyven, T. Liu, M. Xu, M. G. Lozano, P. Woodward-Court, et al., A foundation model for generalizable disease detection from retinal images, *Nature* 622 (2023) 156–163.
- R. Strudel, R. Garcia, I. Laptev, C. Schmid, Seg-menter: Transformer for semantic segmentation, in:

- 2021 IEEE/CVF International Conference on Computer Vision (ICCV), 2021, pp. 7242–7252.
- Y. He, A. Carass, S. D. Solomon, S. Saidha, P. A. Calabresi, J. L. Prince, Retinal layer parcellation of optical coherence tomography images: Data resource for multiple sclerosis and healthy controls, *Data in Brief* 22 (2019) 601–604.
- M. Wiesenfarth, A. Reinke, B. A. Landman, M. Eisenmann, L. A. Saiz, M. J. Cardoso, L. Maier-Hein, A. Kopp-Schneider, Methods and open-source toolkit for analyzing and visualizing challenge results, *Scientific Reports* 11 (2021). URL: <http://dx.doi.org/10.1038/s41598-021-82017-6>. doi:10.1038/s41598-021-82017-6.
- A. Paszke, S. Gross, F. Massa, A. Lerer, J. Bradbury, G. Chanan, T. Killeen, Z. Lin, N. Gimelshein, L. Antiga, A. Desmaison, A. Köpf, E. Yang, Z. DeVito, M. Raison, A. Tejani, S. Chilamkurthy, B. Steiner, L. Fang, J. Bai, S. Chintala, Pytorch: An imperative style, high-performance deep learning library, 2019. URL: <https://arxiv.org/abs/1912.01703>. arXiv:1912.01703.
- V. Andrearczyk, V. Oreiller, S. Boughdad, C. C. Le Rest, O. Tankyevych, H. Elhalawani, M. Jreige, J. O. Prior, M. Vallières, D. Visvikis, M. Hatt, A. Depeursinge, Automatic head and neck tumor segmentation and outcome prediction relying on fdg-pet/ct images: Findings from the second edition of the hecktor challenge, *Medical Image Analysis* 90 (2023) 102972. URL: <https://www.sciencedirect.com/science/article/pii/S1361841523002323>. doi:<https://doi.org/10.1016/j.media.2023.102972>.
- C. I. Nwoye, D. Alapatt, T. Yu, A. Vardazaryan, F. Xia, Z. Zhao, T. Xia, F. Jia, Y. Yang, H. Wang, D. Yu, G. Zheng, X. Duan, N. Getty, R. Sanchez-Matilla, M. Robu, L. Zhang, H. Chen, J. Wang, L. Wang, B. Zhang, B. Gerats, S. Raviteja, R. Sathish, R. Tao, S. Kondo, W. Pang, H. Ren, J. R. Abbing, M. H. Sarhan, S. Bodenstedt, N. Bhasker, B. Oliveira, H. R. Torres, L. Ling, F. Gaida, T. Czempiel, J. L. Vilaça, P. Morais, J. Fonseca, R. M. Egging, I. N. Wijma, C. Qian, G. Bian, Z. Li, V. Balasubramanian, D. Sheet, I. Luengo, Y. Zhu, S. Ding, J.-A. Aschenbrenner, N. E. van der Kar, M. Xu, M. Islam, L. Seenivasan, A. Jenke, D. Stoyanov, D. Mutter, P. Mascagni, B. Seeliger, C. Gonzalez, N. Padoy, Cholectriplet2021: A benchmark challenge for surgical action triplet recognition, *Medical Image Analysis* 86 (2023) 102803. URL: <http://dx.doi.org/10.1016/j.media.2023.102803>. doi:10.1016/j.media.2023.102803.
- R. Dorent, A. Kujawa, M. Ivory, S. Bakas, N. Rieke, S. Joutard, B. Glocker, J. Cardoso, M. Modat, K. Batmanghelich, A. Belkov, M. B. Calisto, J. W. Choi, B. M. Dawant, H. Dong, S. Escalera, Y. Fan, L. Hansen, M. P. Heinrich, S. Joshi, V. Kashtanova, H. G. Kim, S. Kondo, C. N. Kruse, S. K. Lai-Yuen, H. Li, H. Liu, B. Ly, I. Oguz, H. Shin, B. Shirokikh, Z. Su, G. Wang, J. Wu, Y. Xu, K. Yao, L. Zhang, S. Ourselin, J. Shapey, T. Vercauteren, Crossmoda 2021 challenge: Benchmark of cross-modality domain adaptation techniques for vestibular schwannoma and cochlea segmentation, *Medical Image Analysis* 83 (2023) 102628. URL: <http://dx.doi.org/10.1016/j.media.2022.102628>. doi:10.1016/j.media.2022.102628.
- M. R. E. aoun, L. N. Tidjon, B. Rombaut, F. Khomh, A. E. Hassan, An empirical study of library usage and dependency in deep learning frameworks, 2022. URL: <https://arxiv.org/abs/2211.15733>. arXiv:2211.15733.